

### 3.0 SEISMICITY ANALYSES

In this section, we describe analyses of data from the Jackson Lake Seismic Network (JLSN) to develop three-dimensional (3D) velocity models of the crust, earthquake locations, focal mechanisms, and an earthquake catalogue for recurrence analyses. It is necessary to develop a 3D velocity model of the crust to accurately locate earthquakes, to determine focal mechanisms, to perform earthquake declustering for earthquake recurrence analyses, and to estimate ground motion responses in the vicinity of Jackson Lake Dam.

Figure 3-1 shows the geographic distribution of JLSN stations. The network initially consisted of 16 short-period (1 Hz) vertical-component (Geotech model S-13) seismographic stations. An additional four stations were installed in 1990 to improve monitoring coverage, bringing the total to 20 stations. Prior to Oct. 2000, the network used analog telemetry between station sites and communications collection facilities located in the field. The analog signals were relayed to Denver over dedicated phone circuits and digitized using a real-time computer system equipped with a 12-bit digitizer. Data were time-stamped in Denver using either GPS- or GOES-based timing systems. From Oct. 2000 to Oct. 2002, the data were digitized at the communications collection facilities in the field using 16-bit digitizers equipped with GPS time-keeping systems, and then relayed to Denver via local Frame Relay links to Reclamation's wide-area network. This change greatly improved signal-to-noise ratios by reducing analog data transfers to relatively short transmission paths via FM radio between the seismographic stations and the field communications collection facilities. Seven digital broadband three-component velocity seismographs were installed from 1996 to 2001 on-or-near Jackson Lake Dam to provide site response recordings of local earthquakes (Figure 3-2). Four of the site-response stations operated intermittently until the end of Oct. 2002. A detailed description of the original (16-station) short-period seismographic network and instrumentation is found in Wood (1988). The site-response instrumentation is described in Chapter 5 of this report.

From 1986 through 2002, more than 16,000 local earthquakes were recorded by the seismic network, ranging in magnitude from 0.5 to 4.7. Of these earthquakes, about 1,550 were greater than magnitude 2.0. Earthquakes of this size and larger were typically recorded clearly on most of

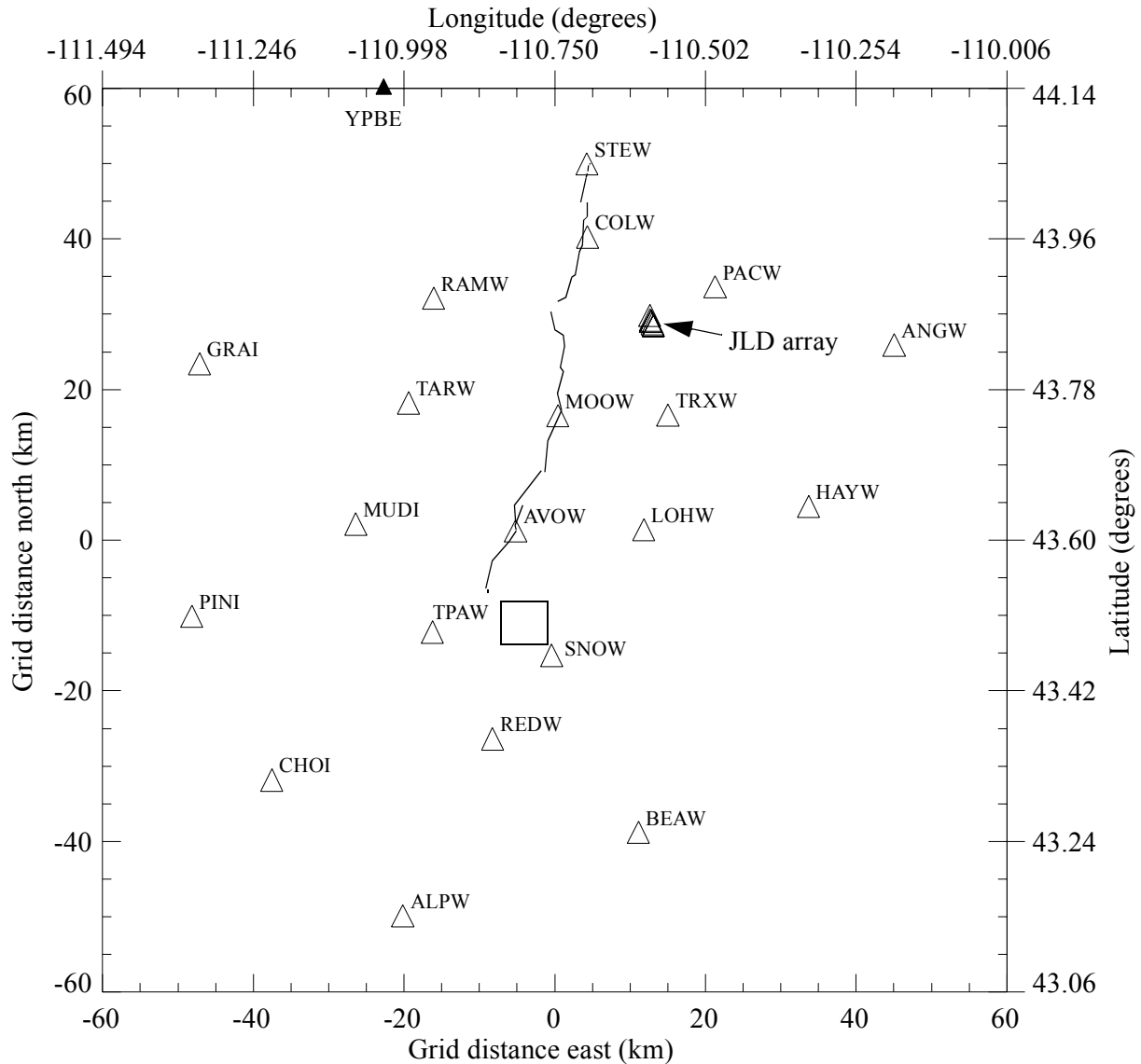


Figure 3-1: Map showing the distribution of JLSN seismographic stations. The filled triangle is station YPBE from the University of Utah Yellowstone seismic network. JLSN stations are open triangles labeled with four-letter station names, the Jackson Lake Dam site response array is the cluster of triangles labeled JLD array, the line segments show the surface traces of the Teton fault, and the town of Jackson is the square. The map coordinates are the Cartesian grid coordinates used in the 3D velocity-hypocenter inversion. The origin of the cartesian grid is 43.6°N, 110.75°W.

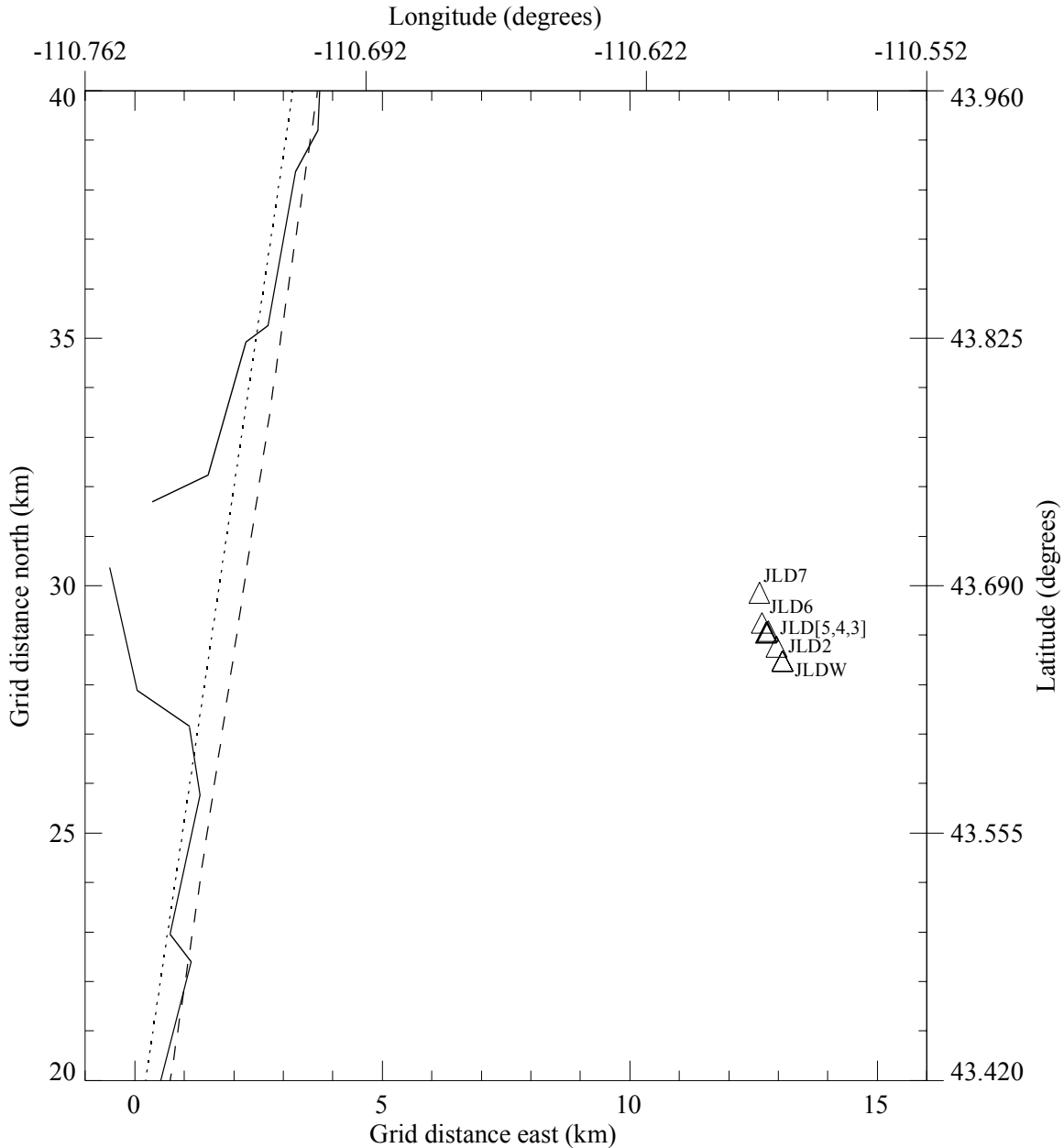


Figure 3-2: Map showing the distribution of Jackson Lake Dam site-response seismographs. Jackson Lake Dam site-response stations are labeled triangles; the designation JLD[5,4,3] refers to station JLD5 on the dam crest, station JLD4 on the eastern dam toe, and station JLD3 located east of the treated foundation zone. The solid line segments show the surface traces of the Teton fault. The dotted line shows the idealized position of the Teton fault used in Section 6 to synthesize ground motions at station JLDW. The dashed line shows that the credible eastern limit for an idealized position of the Teton fault is about 0.5 km closer to the dam than the Teton fault position used in Section 6. The map coordinates are the Cartesian grid coordinates used in the 3D velocity-hypocenter inversion. The rock reference station, JLDW, is located furthest from the idealized Teton fault surface traces at distances of 11.2-to-11.7 km due east of the fault traces. Station JLD7 as located near the northern end of the dam, and is the closest station to the Teton fault at distances of 10.4-to-10.9 km due east of the idealized Teton fault surface traces. Station JLD2 is the station near the dam that is furthest from the Teton fault at distances of 11.1-to-11.6 km due east of the fault traces.

the stations in the seismic network. All earthquakes were automatically processed in real time. Phase arrivals for all local earthquakes equal or greater than magnitude 2, along with selected smaller earthquakes, were subsequently interactively picked and reprocessed. Routine processing included phase picking, magnitude estimation, 1-D hypocenter location, focal mechanism determination, and seismic moment estimation.

### **3.1 Hypocenter-Velocity-Station Correction Inversion**

**3.1.1 Procedure.** A joint hypocenter-velocity-station correction inversion was performed using arrival times from a subset of 1150 earthquakes with well-constrained hypocenters. These events were selected from all events recorded between August, 1986, and May, 2002, having initial locations within the region bounded by the Jackson Lake seismic network. The events were selected using the following criteria: number of stations with arrival times  $\geq 12$ , maximum azimuthal gap  $\leq 160^\circ$ , and distance from epicenter to the nearest recording station divided by the focal depth  $\leq 2$ . The number of events included in the inversion was further reduced using a spatial distribution criteria, in order to limit spatially redundant data and thereby reduce computation time. These 1150 events provided 18,117 P-wave arrival times. S-wave arrival times were not included in the inversion because of a lack of spatially-distributed three-component stations and significant uncertainty about S-wave arrival times determined solely from vertical component seismographs.

Earthquake hypocenters, P-wave velocities, and station corrections varied simultaneously during the inversion. Initially, P-wave velocities were only allowed to vary vertically, and subsequently they were allowed to vary in three dimensions. Station corrections were only included for those stations located outside the 3D velocity grid and for stations JLD2 to JDL7, located on soil sites near Jackson Lake Dam. Arrival times from 40 quarry explosions provided some constraints during the inversion. The z coordinates of these events were fixed at the known elevation of the quarry, while the (x,y) coordinates and origin times varied. Details of the inversion procedure are included in Appendix B.

Following the inversion, 4642 events were relocated with the final 3D P-wave velocity model and station corrections. These events were selected from all recorded events using the following

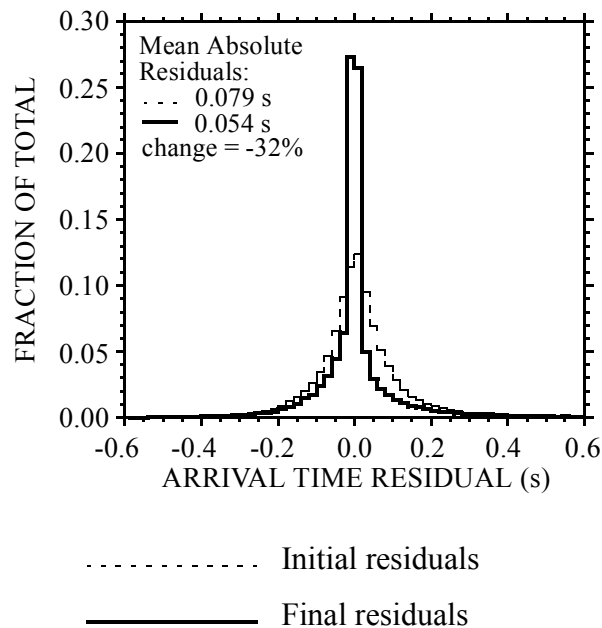


Figure 3-3: Histograms of arrival time residuals. Initial (dashed lines) and final (solid lines) are P-wave residual histograms from 4642 events relocated with the new model from the hypocenter-velocity-station correction inversion.

criteria: number of stations with arrival times  $\geq 6$ , maximum azimuthal gap  $\leq 225^\circ$ , and distance from epicenter to the nearest recording station  $\leq 20$  km.

**3.1.2 Improvement in Residuals.** The 3D P-wave velocity model and corresponding station corrections obtained from the hypocenter-velocity-station correction inversion provide a much better fit to the data than that obtained with the original model. For all relocated events, the mean absolute P-wave arrival time residual decreased by 32% (Figure 3-3).

**3.1.3 New Velocity Model and Station Corrections.** Horizontal slices through the final 3D P-wave velocity model are shown in Figure 3-4. Although velocities were allowed to vary during the inversion from +2 to -16 km elevation (relative to mean sea level), only cross sections at and above -5 km elevation are presented because of a lack of significant horizontal velocity variations below that depth. The discrete-node velocity model (with linearly-interpolated velocities between nodes) used during the inversion was interpolated onto 1 km x 1 km x 1 km constant-velocity pixels for plotting. Pixels that are not crossed by at least one ray path are not

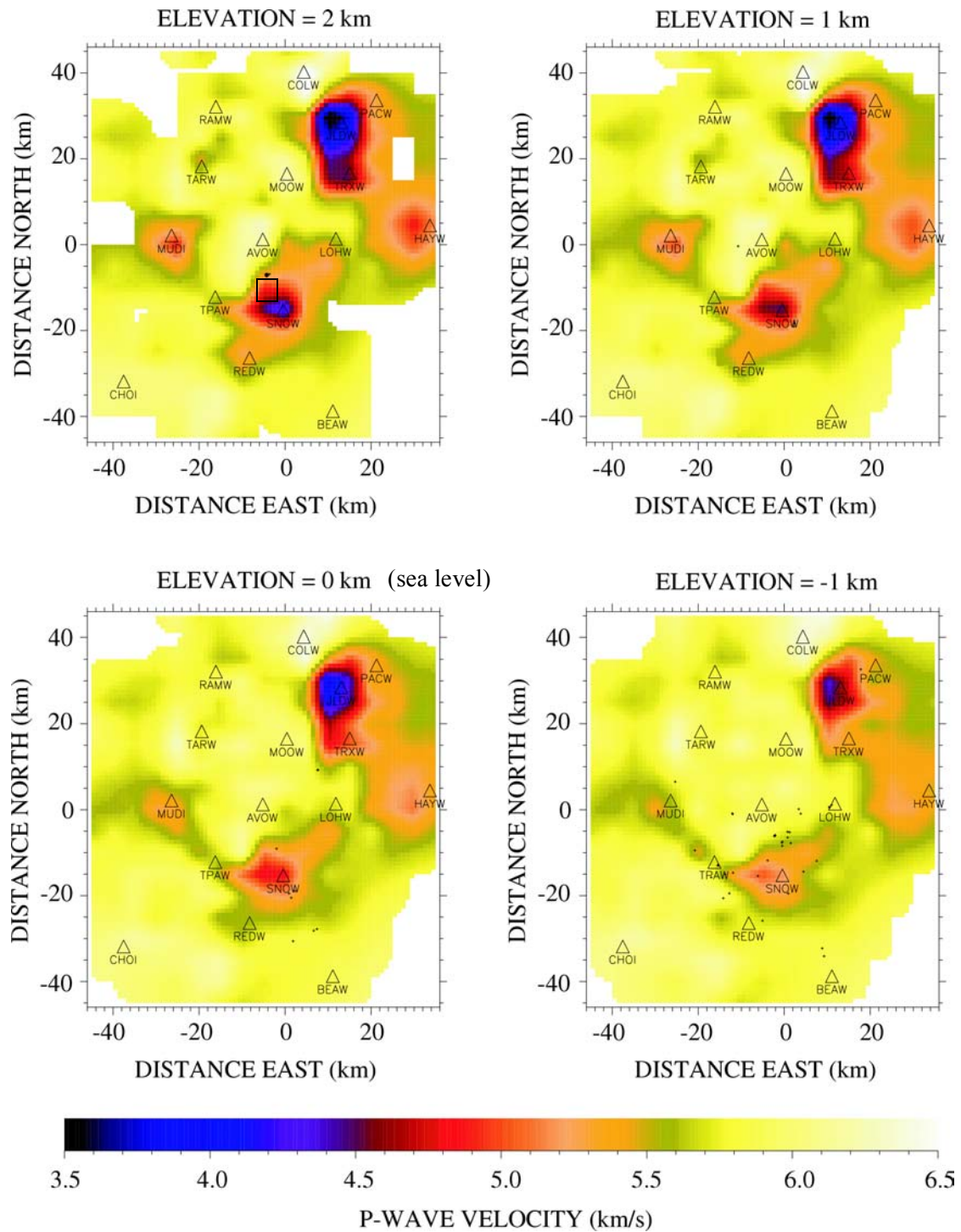


Figure 3-4: Plan views of P-wave velocities for elevations (relative to mean sea level) of -5 km to 2 km. Triangles are seismographic stations. Black pluses are hypocenters within 0.5 km of each the plotted elevation. Regions where velocities are not constrained by ray coverage are shaded white. The town of Jackson, Wyoming, is the black square in the 2 km elevation plot. The plots are continued on the next page.

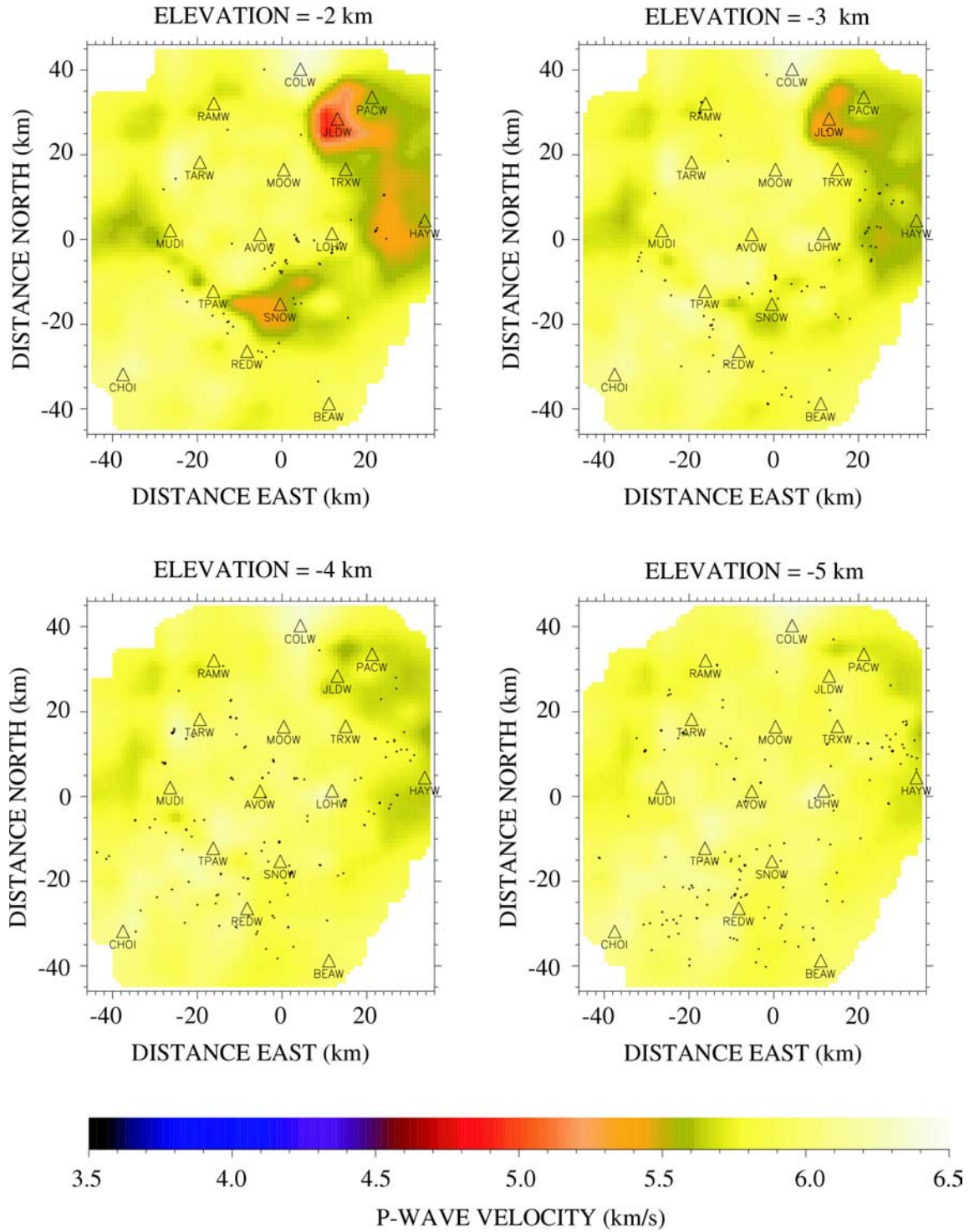


Figure 3-4 continued.

plotted (e.g., these pixels are white). The seismic stations that lie within the 3D velocity grid are shown on the plan-view constant elevation plots for reference. The final locations of the events used in the inversion that occur within 0.5 km of each cross section are also plotted.

Four P-wave low-velocity anomalies are centered near seismic stations JLDW (at Jackson Lake Dam), MUDI, SNOW, and HAYW. The relatively low P-wave velocities occur from the ground surface to at least -2 km elevation. The anomaly around station JLDW, which has the lowest velocities (as low as 3.4 km/s), disappears between -2 and -3 km elevation (between 4.1 and 5.1 km depth). While the shallowest velocities may be vertically smeared due to insufficient ray coverage, the lower boundaries of the velocity anomalies are fairly well-constrained by the data.

The P-wave station corrections obtained from the joint inversion are listed in Table 3-1. Station corrections were included only at stations located outside the 3D velocity grid and at stations JLD2 to JLD7, located on soil sites near Jackson Lake Dam (Figures 3-1 and 3-4). A positive

**Table 3-1: Station corrections from the hypocenter-velocity-station correction inversion.**

STATION NAME	P-WAVE STATION CORRECTION (s)
ALPW	-0.157
ANGW	0.007
GRAI	0.326
PINI	-0.025
STEW	0.102
YPBE	0.022
JLD2	0.036
JLD3	0.041
JLD4	0.026
JLD5	0.053
JLD6	0.043
JLD7	0.031



station correction indicates that velocities along ray paths going to the station are lower than that given by the velocity model, while a negative station correction indicates relatively high velocities. For a station that is located outside the 3D velocity grid, the station correction reflects cumulative velocity variations between the edge of the grid and the station. For stations JLD2 to JLD7, which are located on soil sites within the 3D velocity grid, the positive station corrections indicate that the shallow local velocities are lower than those given by the velocity model. The relative size of the station corrections at stations JLD2 to JLD7 is not solely indicative of the relative velocities of materials beneath these stations because the velocity model also varies laterally across these stations. The velocities in the model decrease from station JLD2 on the south to station JLD7 near the northern end of Jackson Lake Dam.

**3.1.4 Final Earthquake Locations.** The final locations of the 4642 events relocated in the new model are plotted in Figure 3-5. The locations of earthquakes occurring beyond the perimeter of the seismic network are much less well-constrained than those occurring within the network. The seismicity is distributed throughout the network, with some epicenters concentrated in several distinct clusters. A generally low seismicity rate is associated with the northern two-thirds of the Teton fault, a result typical of many western U.S. normal faults (Smith and Arabasz, 1991).

A histogram of the elevations of the final event locations is presented in Figure 3-6. The median event elevation is -4.9 km (with respect to mean sea level). Very few earthquakes occur below -12 km elevation. There is a slight tendency for earthquake elevations to deepen from the north toward the south (Figure 3-7). Earthquakes tend to cluster closer to a Teton fault dipping  $35^\circ$  than for a dip of  $60^\circ$  along the northern segment of the Teton fault (depth cross sections with north coordinates of 20 km and 40 km in Figure 3-7), but the earthquake locations are too diffuse near the Teton fault to draw strong conclusions about fault dip solely from the earthquake locations.

## 3.2 Focal Mechanisms

Focal mechanisms were estimated for 4600 earthquakes from the 4642 events relocated using the 3D velocity model; the 42 blast events were ignored. Based on the criteria used for event selection and relocation, these earthquakes had reasonable seismographic station coverage. Focal

mechanisms were estimated using P-wave first motions and SV/P amplitude ratios from vertical component seismograms in an approach similar to Kisslinger (1980) and Kisslinger et al. (1981), as updated and improved by Anderson and O'Connell (1998) and O'Connell and Unruh (2000), and further improved as described here. A simulated-annealing, downhill-simplex algorithm

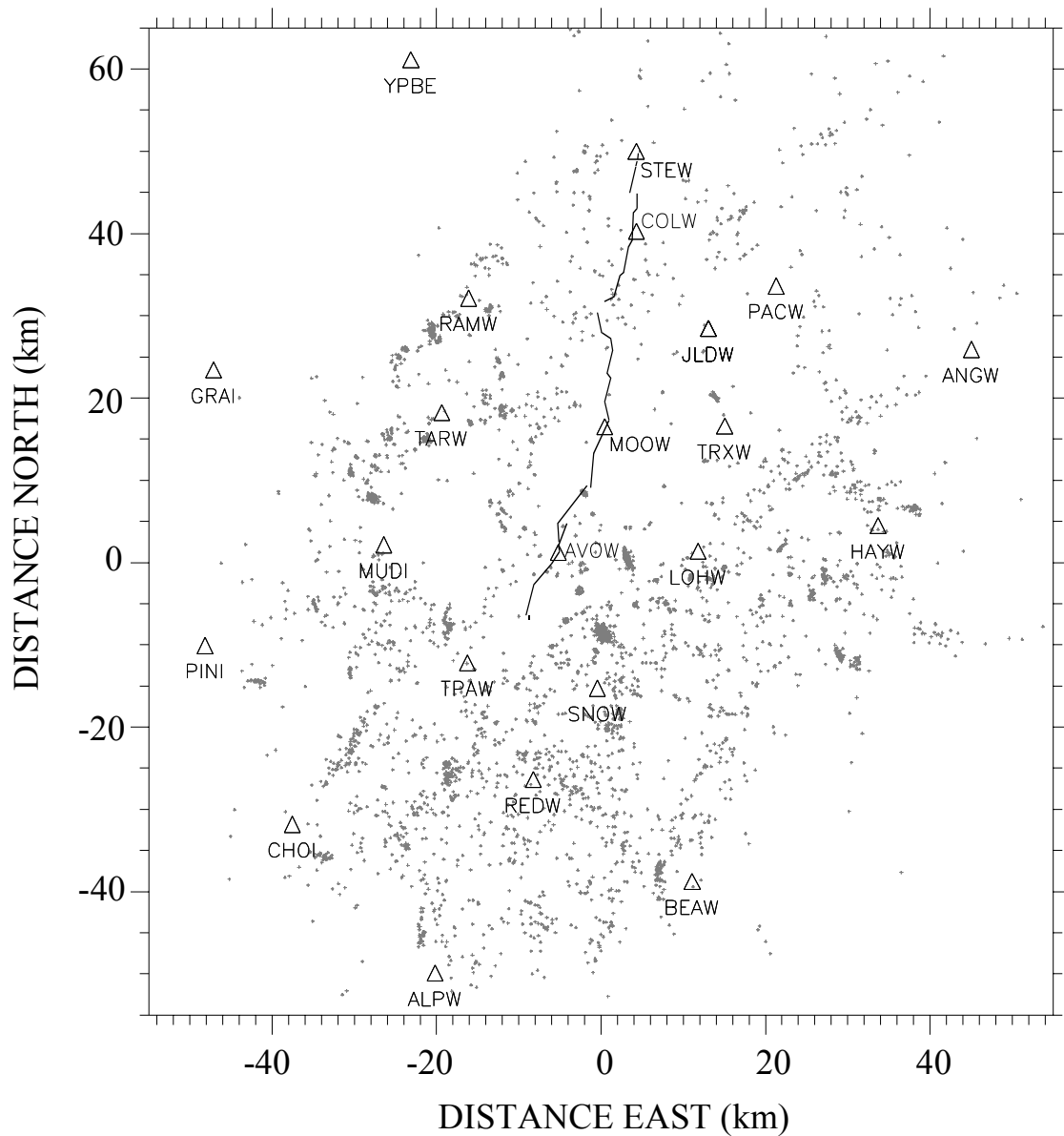


Figure 3-5: Plan view of the final locations of 4642 events relocated in the 3D velocity model from the joint inversion. Triangles are seismographic stations and small grey pluses are the epicenters. The crooked lines show the surface traces of the Teton fault. Station YPBE is part of the Yellowstone seismographic network operated by the University of Utah.

(Press et al., 1992) was used to calculate double-couple focal mechanisms. The starting simplex was constructed to have a normal-faulting node, two strike-slip nodes, and an oblique reverse-faulting node. The first simulated annealing solution was then perturbed four more times to sequentially substitute each of the initial four simplex nodes (one normal, two strike-slip, and one reverse) into the “final” solution simplex to produce four additional focal mechanism solutions. P-wave first motions were weighted 10 times more than SV/P ratio misfits and an L1 norm was used to calculate total misfits. The 20% of the SV/P amplitude ratios with the worst misfit were ignored because SV/P can become unrealistically large near nodal positions. SV/P data from stations at distances greater than 100 km were always ignored in the inversion. SV/P data in the 50 km to 100 km range were linearly downweighted from one to zero, respectively. One second P-wave windows and 5 second S-wave windows were used to calculate integral displacement amplitudes. The velocity seismograms are high-pass filtered with a one pole Butterworth filter at one Hz and double integrated to estimate long-period displacement levels. This method of calculating displacement integral amplitudes was compared to spectral fitting procedures to displacement spectra, and found to be more stable than spectral approaches. A total

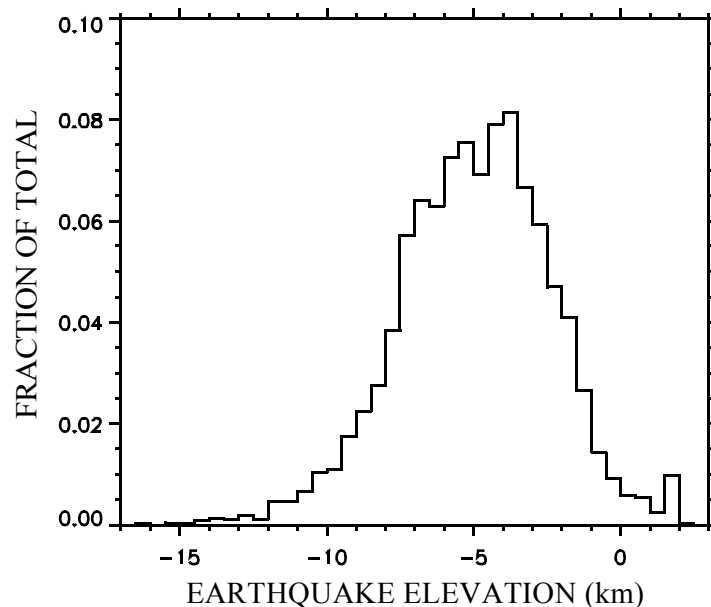


Figure 3-6: Histogram of the final earthquake elevations (with respect to mean sea level, e.g., 0 km). The histogram was constructed using the 4642 events relocated in the 3D velocity model from the joint inversion.

of 28 “temperature” levels were used in the simulated annealing inversions, with a maximum of 90 function evaluations at each “temperature”. The starting “temperature” was set to a value corresponding to 60 misfitting first motions and decreased using the following temperature schedule,  $T = T_0(1-k/K)^\alpha$ , where  $T_0$  is the initial temperature,  $K$  is the total number of function evaluations, and  $k$  is the cumulative number of function evaluations so far, and  $\alpha$  is set to two. At large “temperatures”, the process occasionally accepts models associated with increases in functional misfit to inhibit convergence to a local minima. As  $T$  tends toward zero, the inversion reduces to a simple downhill simplex algorithm (Press et al., 1992). Take-off angles and azimuths were calculated using the 3D P-wave velocity model curved ray paths. S waves were assumed to follow the same ray paths as the P waves.

Given the large number of earthquakes, numerical criteria were used to determine the subset of earthquakes with well-constrained focal mechanisms. A minimum of 8 P-wave first motions, and a total of at least 12 P-wave first motions and SV/P amplitude ratios were required to retain an earthquake for focal mechanism analysis. Since five candidate focal mechanism solutions were available for each earthquake, a criteria for a robust solution is that one of the five focal mechanism solutions fit the data distinctly better than the other four solutions, or that all five solutions fit nearly equally well and are essentially the same. Any solution that had a likelihood 2/3 or greater of the best-fitting solution was considered to fit the data equally well as the “best-fitting” solution. If the  $T$ -axis azimuths of nearly-equally-fitting solutions varied either  $< 5^\circ$  or  $< 20^\circ$ , the solutions were considered similar and well constrained. Two scenarios were used for the  $T$ -axis variability criteria to evaluate sensitivity to this criteria. A  $5^\circ$   $T$ -axis azimuth variability cutoff yields 307 focal mechanisms, but is probably too conservative, and limited the geographic distribution and density of focal mechanisms (Figure 3-8). A  $20^\circ$   $T$ -axis azimuth variability cutoff produces 773 focal mechanisms and a more detailed distribution of focal mechanisms, but may include a small percentage of focal mechanisms that are not well constrained or are even erroneous (Figure 3-9);  $T$ -axes standard deviations are slightly larger when  $T$ -axis variability is allowed to be  $< 20^\circ$  (compare Figures 3-9 and 3-8), but the overall pattern is very similar.

The focal mechanisms were divided into five focal mechanism classes based on  $T$ - and  $P$ -axis plunges ( $T_p$  and  $P_p$ , respectively), as defined in Tables 3-2 and 3-3. For the well-constrained focal

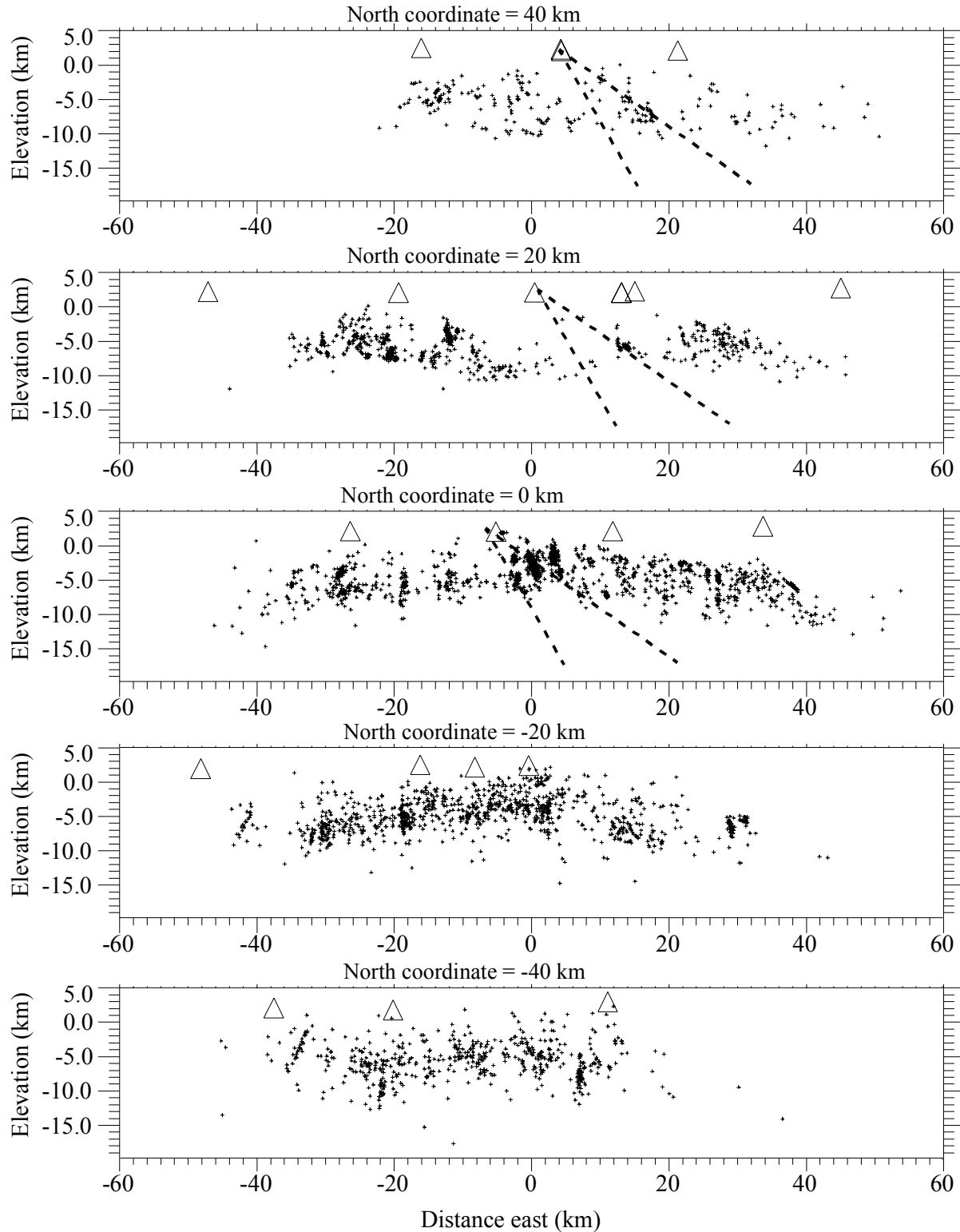


Figure 3-7: West-east depth sections of earthquake locations. Earthquakes located within 10 km of the north coordinate (as defined in Figure 3-5) are included in the section as small plus symbols as are seismographic stations as triangles. Where the Teton fault intersects the depth section the fault is shown with dips of 35° and 60° as dashed lines.

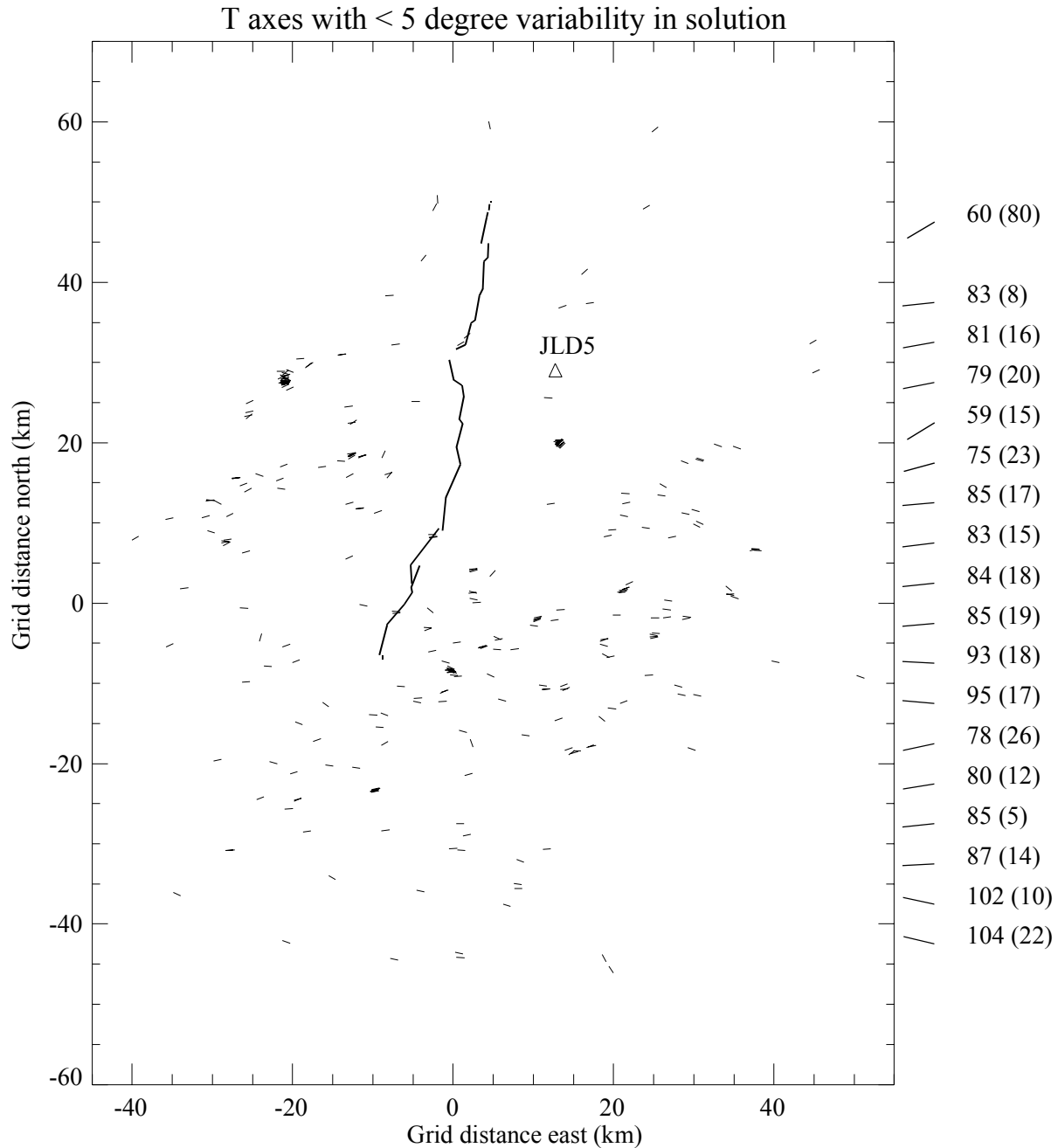


Figure 3-8: *T*-axes azimuths from the 303 focal mechanisms with < 5° *T*-axis solution variability. Each *T* axis is plotted as a 1 km line segment. The thick discontinuous black line segments are the surface traces of the Teton fault. Line segments to the right of the figure show median *T*-axis orientations for east-west regions that are 5-km-wide in the north-south extent labeled by the median *T*-axis azimuth values in degrees east of north and standard deviations in parenthesis. The grid origin corresponds to 43.6°N, 110.75°W. The triangle labeled JLD5 shows the location of the tallest section of Jackson Lake Dam, where site response station JLD5 was located.

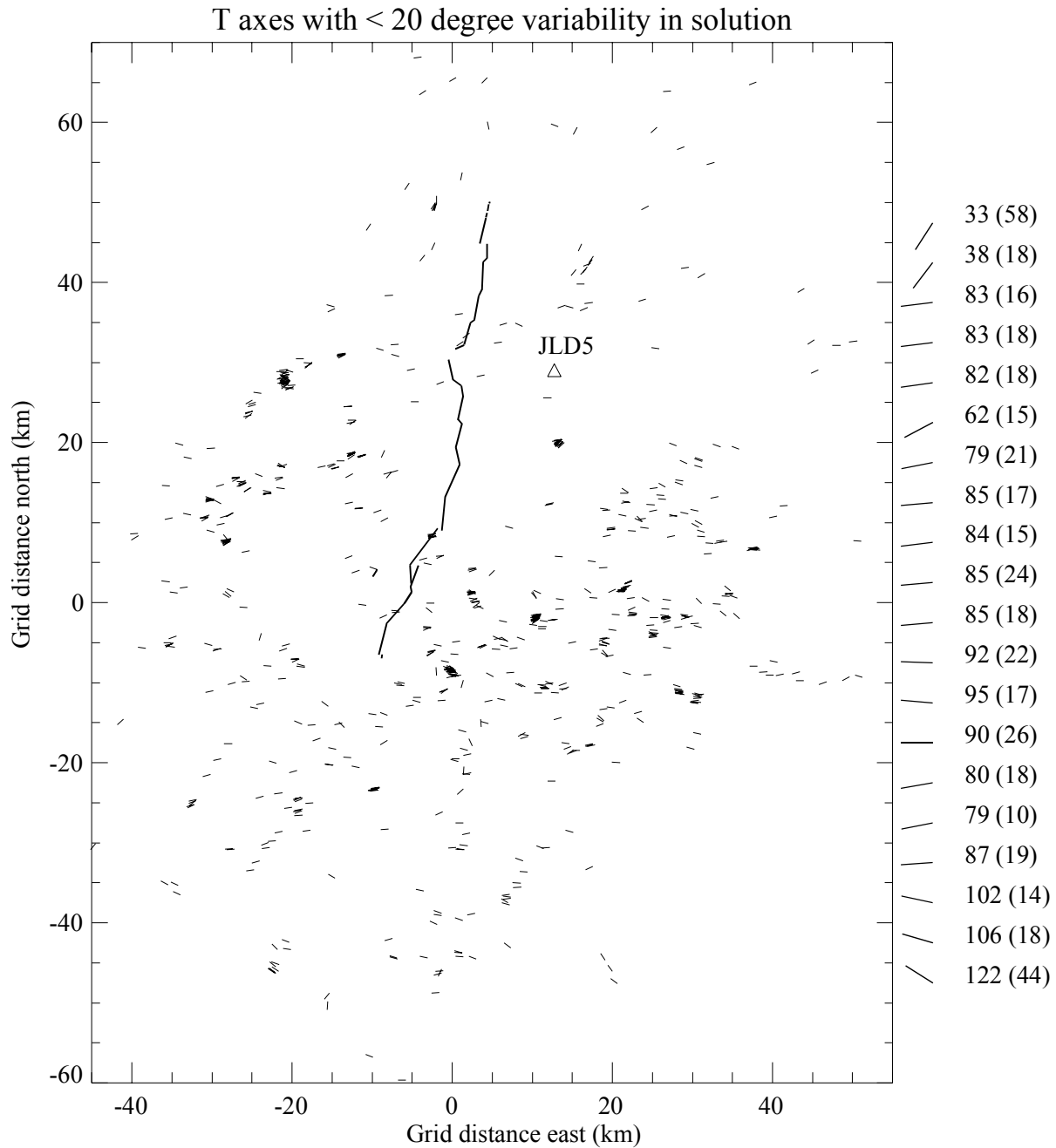


Figure 3-9: *T*-axes azimuths from the 773 focal mechanisms with < 20° *T*-axis solution variability. Each *T* axis is plotted as a 1 km line segment. The thick discontinuous black line segments are the surface traces of the Teton fault. Line segments to the right of the figure show median *T*-axis orientations for east-west regions that are 5-km-wide in the north-south extent labeled by the median *T*-axis azimuth values in degrees east of north and standard deviations in parenthesis. The grid origin corresponds to 43.6°N, 110.75°W. The triangle labeled JLD5 shows the location of the tallest section of Jackson Lake Dam, where site response station JLD5 was located.

**Table 3-2: Number of Different Focal Mechanisms for  $< 5^\circ$   $T$ -axis Azimuth Variability.**

Strike-slip.	Normal.	Reverse.	Oblique Normal.	Oblique Reverse.
$T_p \geq 30 \text{ \& } P_p \leq 30$	$T_p > 60$	$P_p > 60$	$P_p \leq 30 \text{ \& } T_p \geq 30$ $\text{ \& } T_p \leq 60$	$T_p \leq 30 \text{ \& } P_p \geq 30$ $\text{ \& } P_p \leq 60$
160	59	2	69	10

**Table 3-3: Number of Different Focal Mechanisms for  $< 20^\circ$   $T$ -axis Azimuth Variability.**

Strike-slip.	Normal.	Reverse.	Oblique Normal.	Oblique Reverse.
$T_p \geq 30 \text{ \& } P_p \leq 30$	$T_p > 60$	$P_p > 60$	$P_p \leq 30 \text{ \& } T_p \geq 30$ $\text{ \& } T_p \leq 60$	$T_p \leq 30 \text{ \& } P_p \geq 30$ $\text{ \& } P_p \leq 60$
368	172	3	169	34

mechanisms with  $< 5^\circ$   $T$ -axis azimuth variability, these five focal mechanism classes accounted for 300 of the 307 total focal mechanisms. Figure 3-10 shows the “pure” mechanisms (first three columns of Table 3-2). Figure 3-11 shows the “pure” strike slip and oblique mechanisms (first column and last two columns in Table 3-2). For the less well-constrained focal mechanisms with  $< 20^\circ$   $T$ -axis azimuth variability, these five focal mechanism classes accounted for 746 of the 773 total focal mechanisms, and are plotted in Figure 3-12 for “pure” mechanisms (first three columns of Table 3-3) and “pure” strike slip and oblique mechanisms in Figure 3-13 (first column and last two columns in Table 3-3).

The strike-slip, normal-slip, and oblique normal-slip focal mechanisms represent  $> 92\%$  of the focal mechanisms and occur throughout the study area (Figures 3-10 to 3-13). Consequently, the  $T$ -axes orientations provide the most consistent picture of stress orientation (Figures 3-8 and 3-9).  $T$ -axes are nearly uniformly orientated almost east-west from north grid coordinate -35 km to 40 km.  $T$ -axes azimuths turn more northerly along the northernmost 10 km of the Teton fault (Figure 3-9), possibly reflecting the influence of the Yellowstone region on stresses in the northern portion of the study area. South of -40 km north grid distance,  $T$ -axes azimuths increasingly trend southerly in the southward direction (Figure 3-9). The northeast deflection of the  $T$ -axes at the northern limits of the grid and the southeast deflection of the  $T$ -axes at the southern limits of the



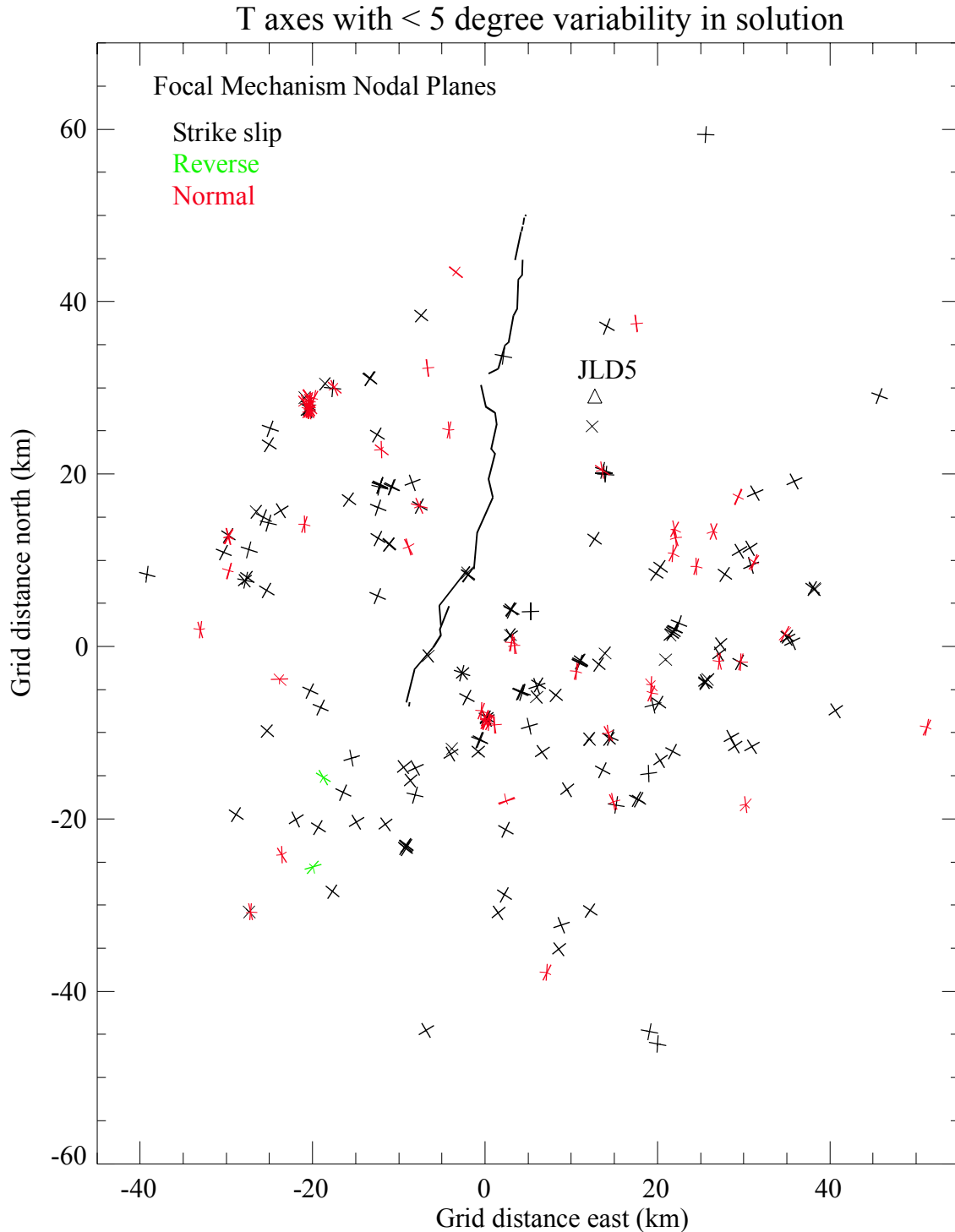


Figure 3-10: “Pure” nodal planes from focal mechanisms with  $< 5^\circ$  T-axis solution variability. The long axes show nodal plane strikes, color-coded by focal mechanism (see legend on plot) as defined in Table 3-2. The short orthogonal lines show dip directions for the normal and reverse mechanisms; dip lines are half nodal strike lengths for a dip of zero and have zero length for a dip of  $90^\circ$ . The grid origin corresponds to  $43.6^\circ\text{N}$ ,  $110.75^\circ\text{W}$ . The thick discontinuous black line segments are the surface traces of the Teton fault. The triangle labeled JLD5 shows the location of the tallest section of Jackson Lake Dam, where site response station JLD5 was located.

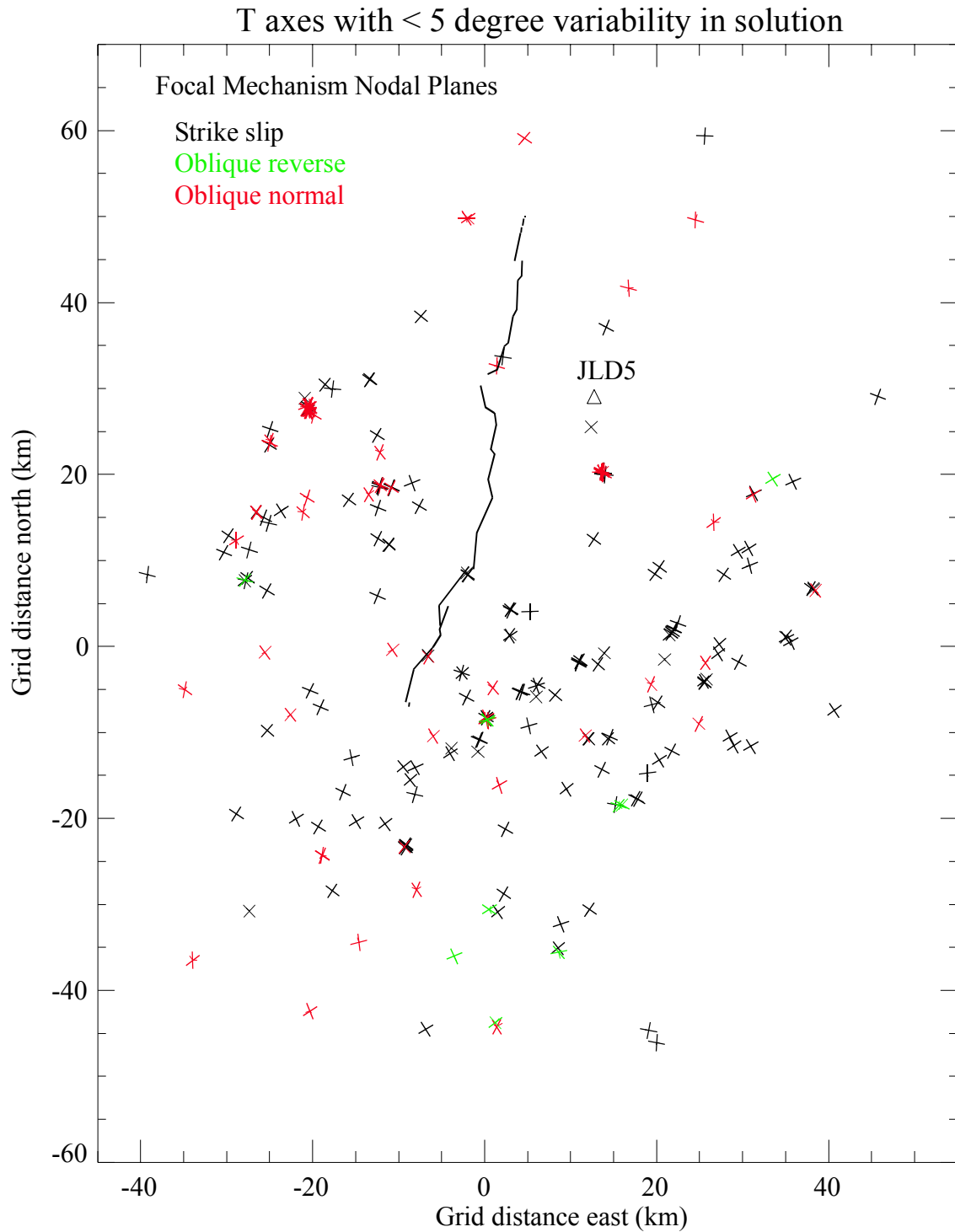


Figure 3-11: “Pure” strike-slip and oblique dip-slip nodal planes from focal mechanisms with < 5° T-axis solution variability. See Table 3-2 for focal mechanism definitions and Figure 3-10 for plot description.

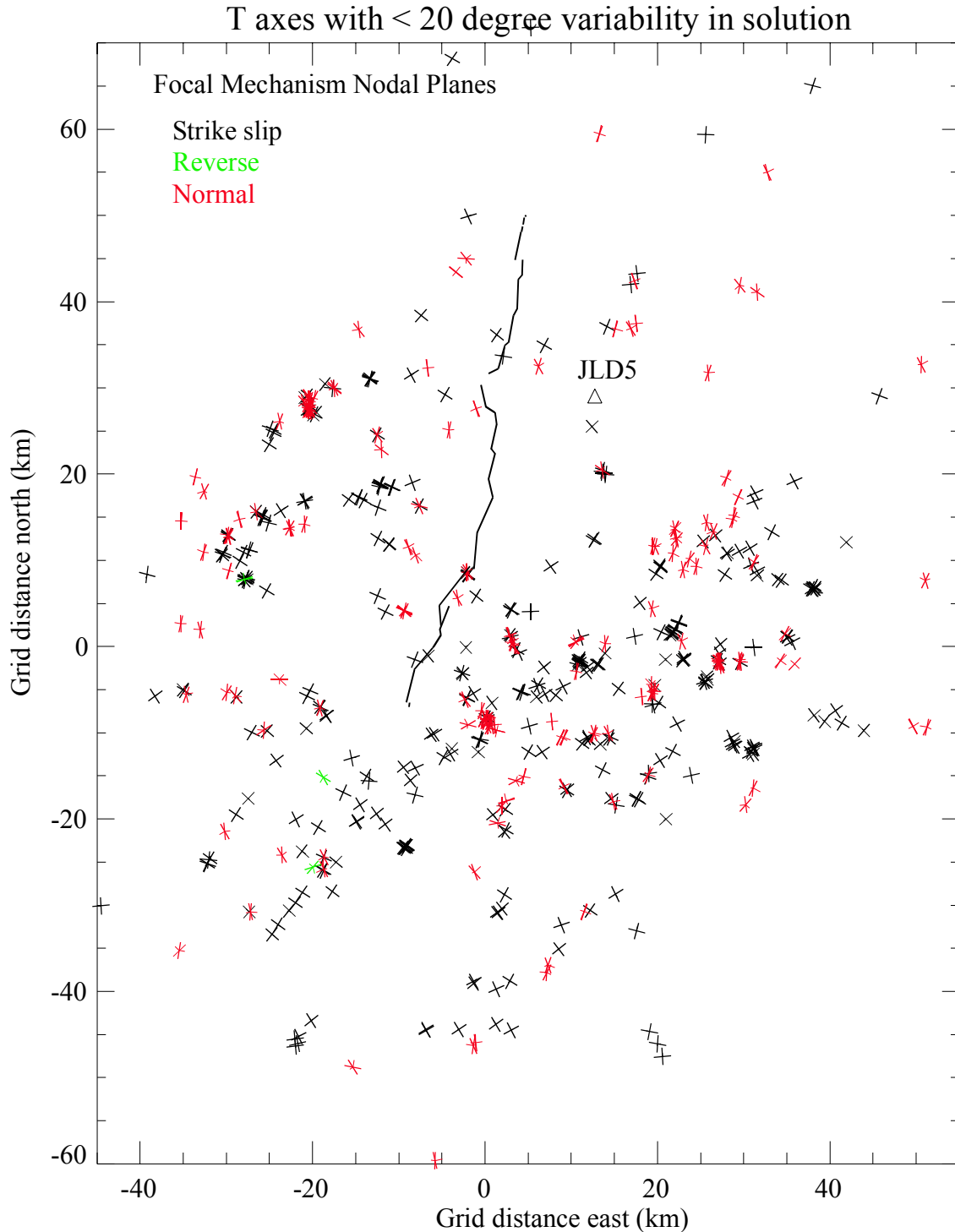


Figure 3-12: “Pure” nodal planes from focal mechanisms with < 20° T-axis solution variability. The long axes show nodal plane strikes, color-coded by focal mechanism (see legend on plot) as defined in Table 3-3. The short orthogonal lines show dip directions for the normal and reverse mechanisms; dip lines are half nodal strike lengths for a dip of zero and have zero length for a dip of 90°. The grid origin corresponds to 43.6°N, 110.75°W. The thick discontinuous black line segments are the surface traces of the Teton fault. The triangle labeled JLD5 shows the location of the tallest section of Jackson Lake Dam, where site response station JLD5 was located.

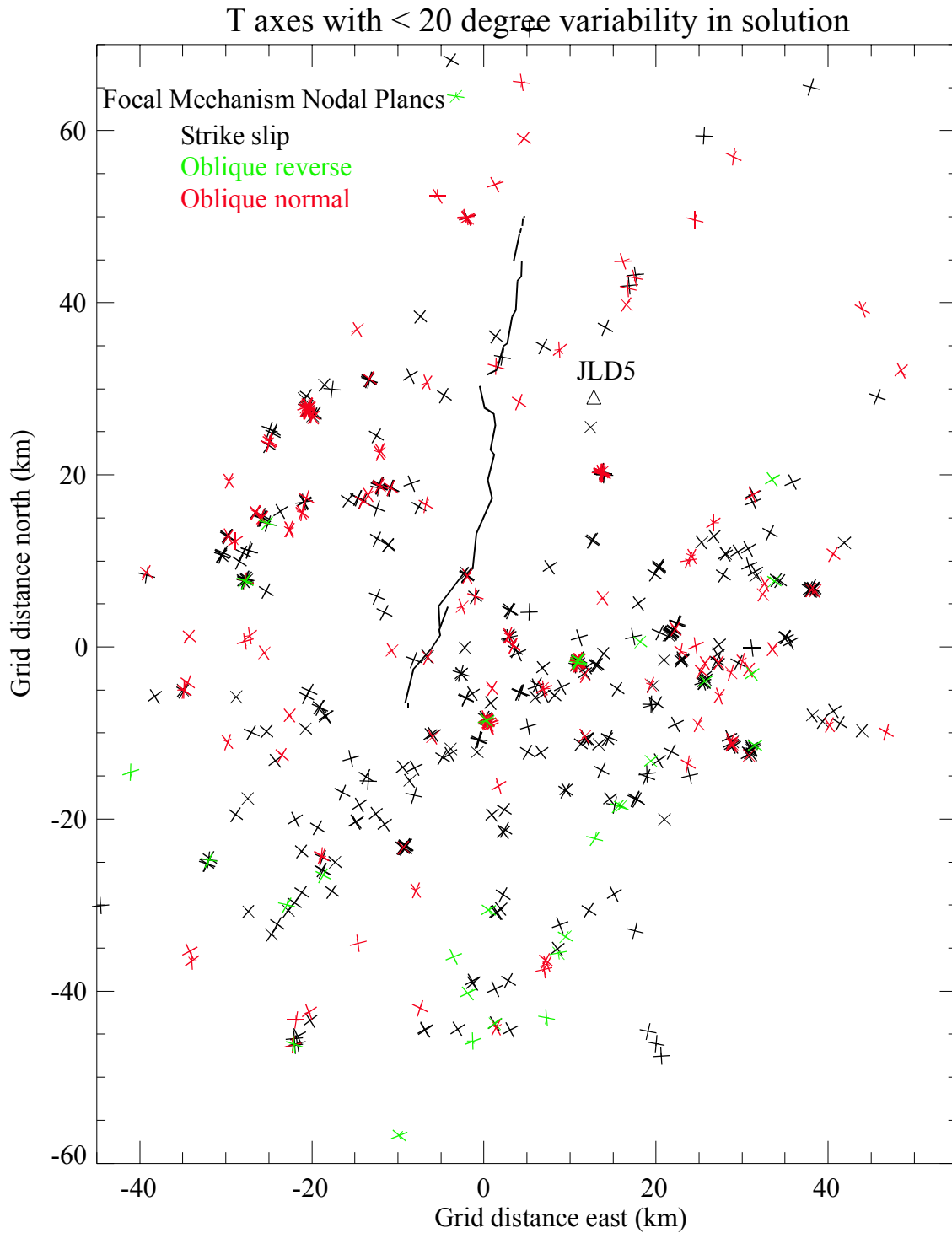


Figure 3-13: “Pure” strike-slip and oblique dip-slip nodal planes from focal mechanisms with < 20° T-axis solution variability. See Table 3-3 for focal mechanism definitions and Figure 3-12 for plot description.

grid roughly maintain the  $T$ -axes normal to the overall parabolic distribution of seismicity east of the Snake River Plain described in Anders et al. (1989). The reverse and oblique reverse solutions are mostly confined to the region south of 15 km north grid coordinates, and may reflect stress heterogeneity in the stepover region between the Teton fault and normal faults south of the Teton fault (e.g., Grand Valley fault and Star Valley fault). Consistent with field observations discussed in Section 2, the  $T$ -axes and nodal planes indicate primarily normal-slip on the central and northern sections of the Teton fault, and oblique left-lateral normal slip on the southern section of the Teton fault. The focal mechanism data, particularly the  $T$ -axes orientations, support using a dominantly normal-slip rake to simulate ground motions associated with rupture of the central and northern segments of the Teton fault.

The relative paucity of earthquakes that could be associated with the Teton fault at depth do not provide strong constraints on fault dip. Focal mechanism solutions of earthquakes located east of the surface trace of the Teton fault dips have east-dipping nodal planes that dip from  $25^\circ$  to  $60^\circ$ . There are too few earthquakes located east of the Teton fault, with far too limited spatial coverage to provide a strong constraint on fault dip, although the spatial distribution of earthquakes is consistent with dips of  $< 50^\circ$  (Figure 3-7). As discussed in Section 4, detailed waveform modeling of two earthquakes suggest that the Teton fault dips  $< 50^\circ$ , if the earthquakes are actually located on the Teton fault. Waveform modeling of more of the earthquakes located east of the Teton fault may provide better constraints on Teton fault dip at depth than are currently available.

### 3.3 Earthquake Recurrence

This section describes the development of earthquake recurrence parameters for the Jackson Lake region. There are two data sets available for this purpose; the Jackson Lake Seismic Network (JLSN) catalog (June, 1986 - December, 2001), and the historic record for this region prior to the network's installation in 1986 (1963 - May, 1986). Two sets of recurrence parameters were developed, one with just the JLSN data and one with the combined JLSN - pre-1986 information. Because few, if any, earthquakes in either catalog have been positively associated with a known fault, this seismicity represents "random" or "background" earthquakes, and any further analysis using the parameters developed here pertain only to such seismic activity.

The procedure consisted of declustering both catalogs in order to qualify as a Poissonian process; one that is random in space and time. Log-normal maximum likelihood magnitude-frequency curves were then fit to the data. Formal uncertainties in recurrence parameter values and seismicity rates were also computed and are presented below.

### 3.4 Catalog Development

#### 3.4.1 Jackson Lake Network Catalog.

The JLSN catalog, with a lower magnitude cutoff of 2.0, consists of 1547 earthquakes (Figure 3-14). The seismicity has a roughly uniform geographic distribution, with decreased activity in the vicinity of the Teton Range and the basin containing Jackson Lake. The largest event is a  $M_c$  (coda magnitude) 4.7 event that occurred on December 28, 1993 (labeled along the right side of Figure 3-14). There are a number of spatial earthquake clusters, the most notable being a swarm in the southwest corner of Figure 3-14. This cluster does not represent a typical mainshock-aftershock sequence, but a series of about 100 events that occurred between November 10 and November 17, 1992. The largest magnitude was 4.0.

**3.4.1.1 Declustering.** In order to model earthquake occurrence as a random process, the catalogs must approximate random space-time characteristics. However, due to the existence of foreshock-mainshock-aftershock sequences and swarms, the raw data set cannot be considered to have “random” or Poissonian characteristics. It is therefore necessary to identify and delete “dependent” events from swarms and foreshock-mainshock-aftershock sequences. A declustering algorithm based on Reasenber (1985) was used for this purpose. This technique, with some modifications, was used by Savage and dePolo (1993) to search for foreshocks in the Nevada seismicity catalog. The algorithm used in this report is based on these two papers, with some additional appropriate modifications. The major details are described below.

Any cluster identification scheme must establish criteria for deciding whether neighboring events in the catalog are “dependent” on or “independent” in time and space. To determine spatial dependence, a “mainshock” is defined, with a magnitude-dependent source radius based on the circular crack model described in Kanamori and Anderson (1975) and a stress drop of 30 bars (a reasonable stress drop for an extensional environment, see Spudich et al., 1999). The radius of the

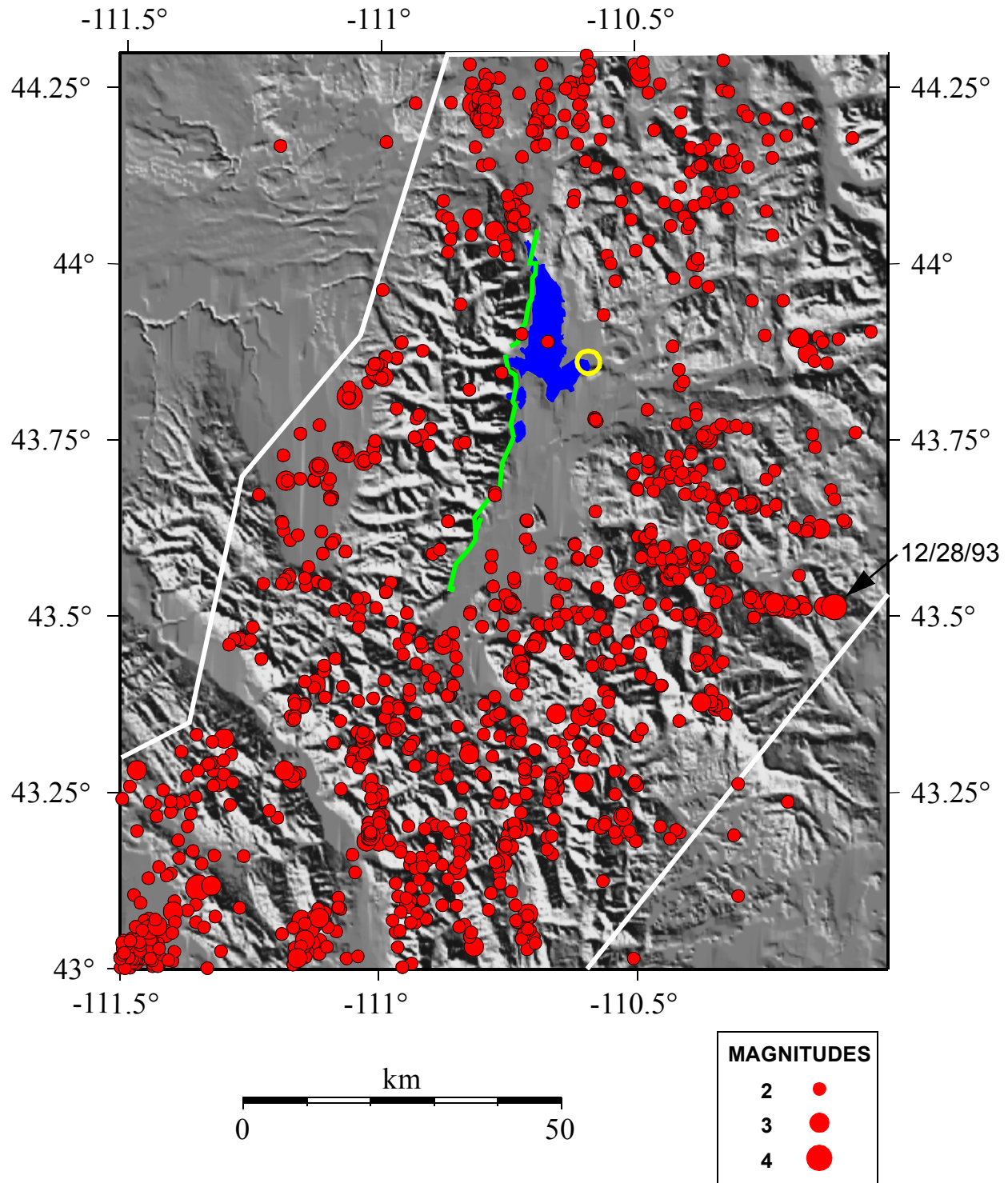


Figure 3-14: Epicenters from Jackson Lake Seismic Network, magnitude  $\geq 2.0$ , June 1986 - December 2001. Surface traces of the Teton fault are shown in green. Location of Jackson Lake Dam shown as yellow circle. Boundaries of recurrence study area shown in white. The arrow points to the location of  $M_c$  4.7 event of Dec. 28, 1993.

next event in time is defined as its circular crack radius times a factor  $Q$ . If the distance between the two epicenters is less than the sum of the two radii, the two events are considered spatially dependent. Temporal dependence is judged by an application of Omori's Law, which describes the exponential temporal decay of aftershocks. The aftershock sequence is modeled as a time-dependent Poisson process, with the Omori constants taken from the "generic Utah model" of Arabasz and Hill (1996). These constants were derived from 10 mainshock-aftershock sequences from the Intermountain Seismic Belt (ISB) in Utah, and are assumed to be representative of aftershock sequences occurring in the study area.

The "look-ahead" time criterion is a function of the Omori constants, the magnitude of the mainshock, the detection threshold magnitude, the confidence probability, and the time between the two events. Since the "look-ahead" time,  $\tau$ , is proportional to the time difference, upper and lower bounds must be placed on it. If the time difference is less than  $\tau$ , the two events are considered temporally dependent. If both spatial and temporal criteria are satisfied, the two events are considered dependent. If the magnitude of the second event exceeds that of the first, it is considered the new mainshock.

Because Reasenber (1985) applied this technique to a catalog resulting from a spatially and temporally uniform seismograph network, it was not necessary to be concerned with changes in earthquake location capabilities through time. During the time span of the JLSN catalog, (1986-2001) we use earthquakes of magnitude 2 and greater, and it was assumed that the catalog is complete down to this magnitude level for the period of network operation. The hypocentral precision was estimated to be 10 km. This means that in judging distance criteria, two events were spatially linked if less than 10 km apart. For a given cluster an "equivalent" event was calculated as the moment-weighted mean of latitude, longitude, and origin time. In contrast to Reasenber (1985), "equivalent" magnitudes, derived by summing the seismic moment of groups of a cluster and finding a new magnitude, were not computed. In our judgement, for purposes of hazard estimation it is more important to retain accurate magnitude estimates than to conserve the seismic moment of the catalog. All other declustering parameters were set to the values recommended in Reasenber (1985).



Space-time plots of the raw and declustered catalog are shown in Figures 3-15 and 3-16. The “a” figures shows latitude vs. time; the “b” figures longitude vs. time. The plots for the unfiltered catalog show many clusters, the most prominent being the 1992 sequence. The plots of the declustered catalog show a much more “random” appearance. There is still a trace of the 1992 swarm in Figure 3-16b, but it is clear from these figures that the great majority of the events have been removed. The events identified as being members of clusters are shown in Figure 3-17. The events that appear to be solitary are actually two or more events at the same location.

Out of a total of 1547 events in the  $M > 2$  JLSN earthquake catalog, 791 events were identified as being members of a total 229 clusters. The number of “independent” earthquakes is 984. The declustered JLSN catalog is shown in Figure 3-18.

### **3.4.2 Pre-Jackson Lake Network Catalog.**

Earthquakes that occurred in the study region prior to installation of the JLSN were also analyzed. These were taken from the Northern California Earthquake Data Center (NCEDC), which compiles earthquake data from a variety of sources. A total of 155 events of magnitude 2 and greater, spanning 1963 to June 1986, were extracted. These data are of lower location accuracy than the JLSN data, due to the sparseness and heterogeneity of seismograph station deployment that predates the installation of the JLSN. Listed magnitudes are either local magnitude ( $M_L$ ), coda magnitude ( $M_c$ ), body wave magnitude ( $M_b$ ), or unknown. This mix of scales signifies probable incompatibility between the values presented. Due to the complexities involved and the scope of this project, no attempt was made to fit the pre-network magnitudes to a common scale, or calibrate them to the JLSN magnitudes.

The pre-network events are plotted in Figure 3-19. The spatial pattern appears similar to the JLSN data (Figure 3-14). The largest event is a  $M_c$  5.1 event that occurred at the top of Figure 3-19 on March 30, 1973.

Declustering was performed on the pre-network catalog, using the same algorithm as described above. Completeness was assumed to magnitude 4, and location precision was estimated to be 20

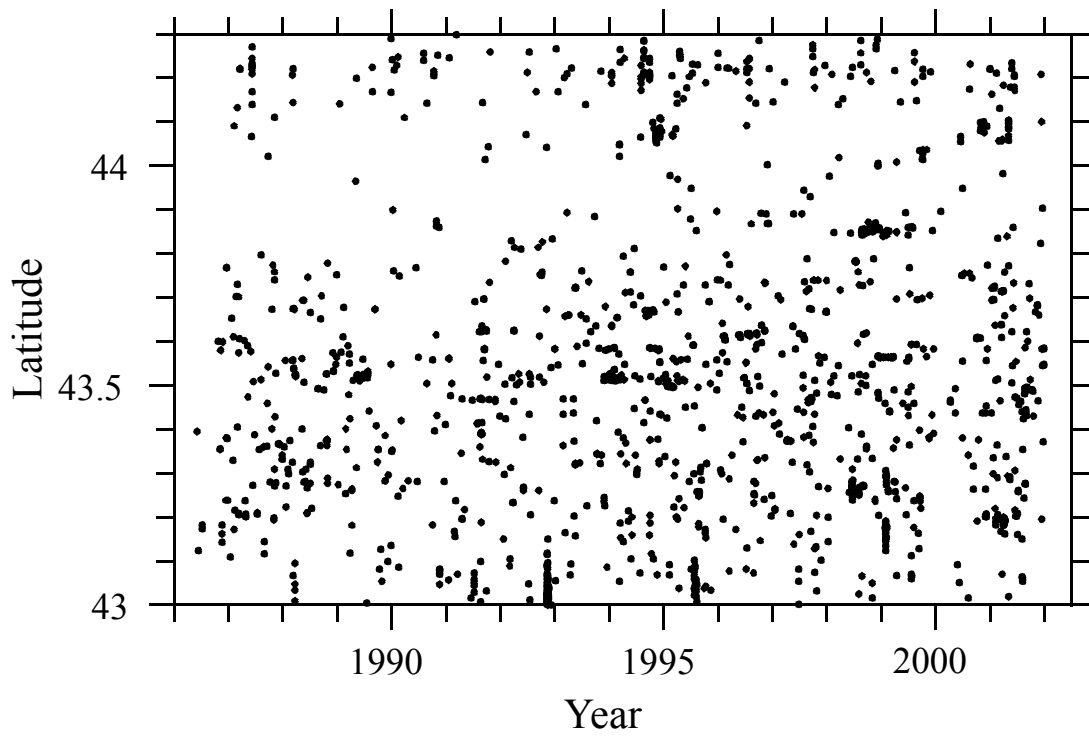


Figure 3-15a: Latitude vs. time, unfiltered JLSN catalog.

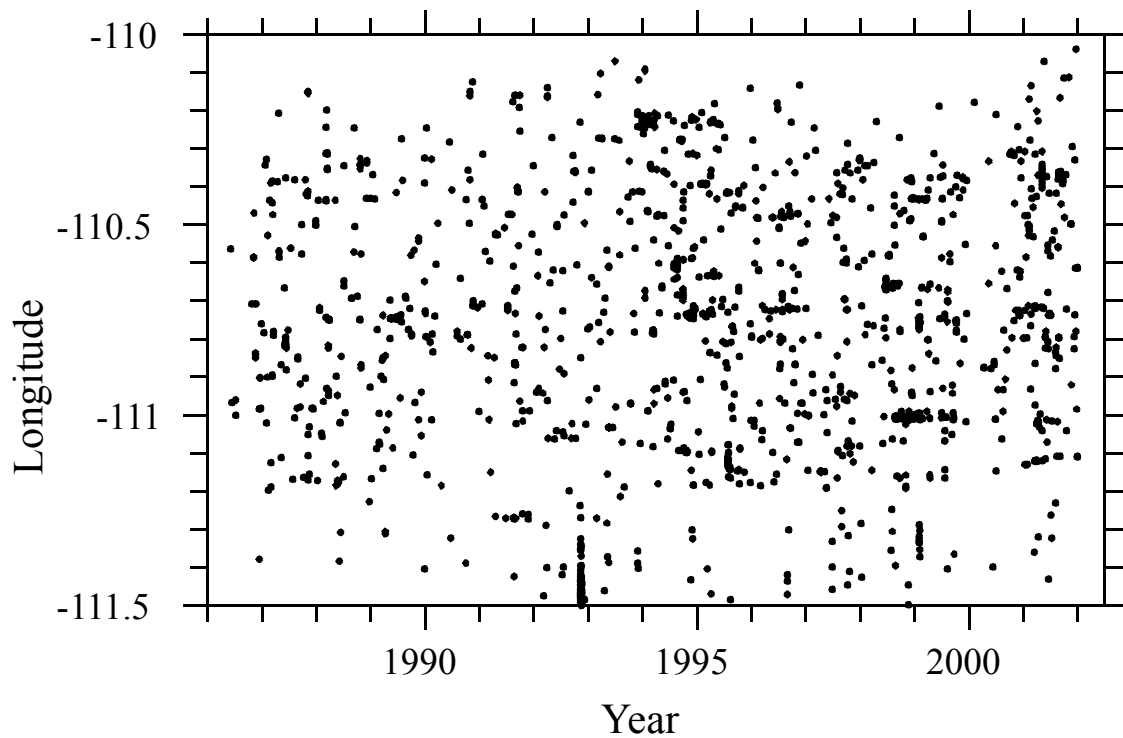


Figure 3-15b: Longitude vs. time, unfiltered JLSN catalog.

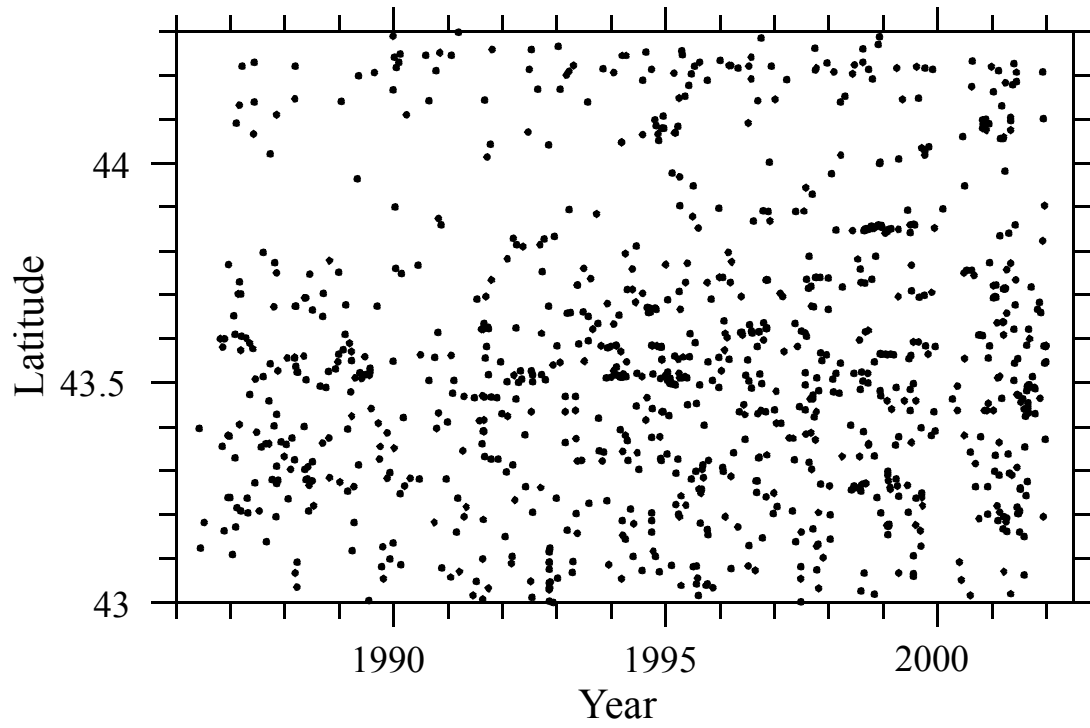


Figure 3-16a: Latitude vs. time, declustered JLSN catalog.

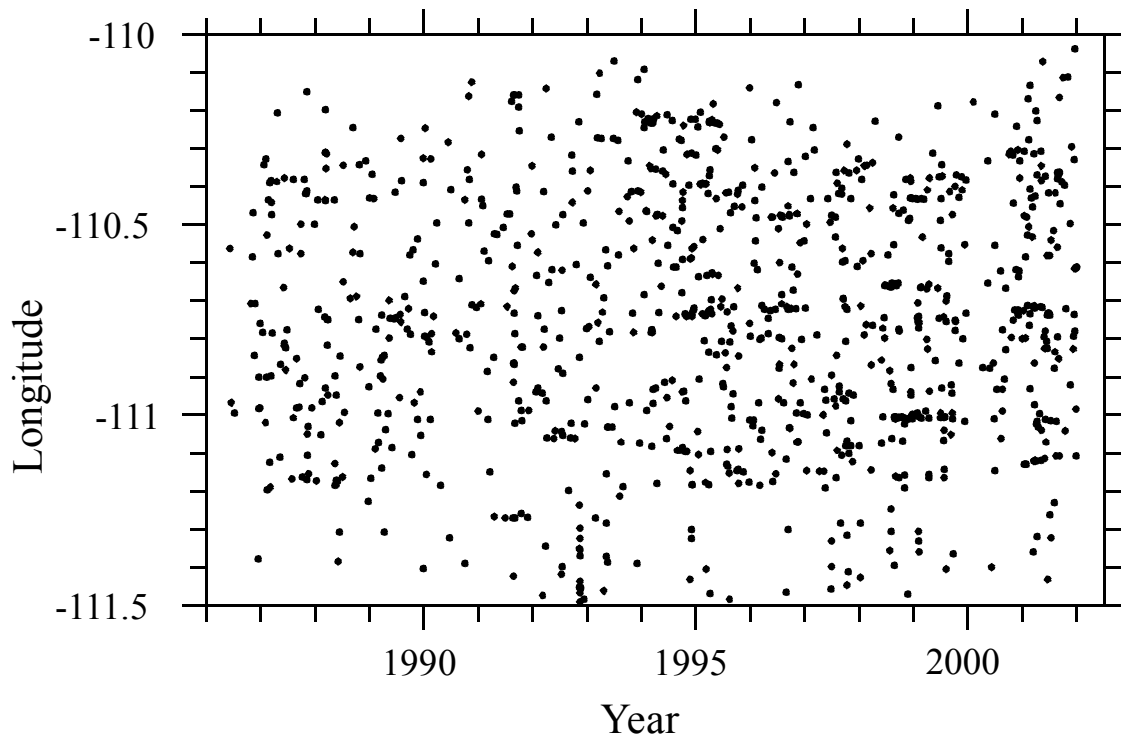


Figure 3-16b: Longitude vs. time, declustered JLSN catalog.

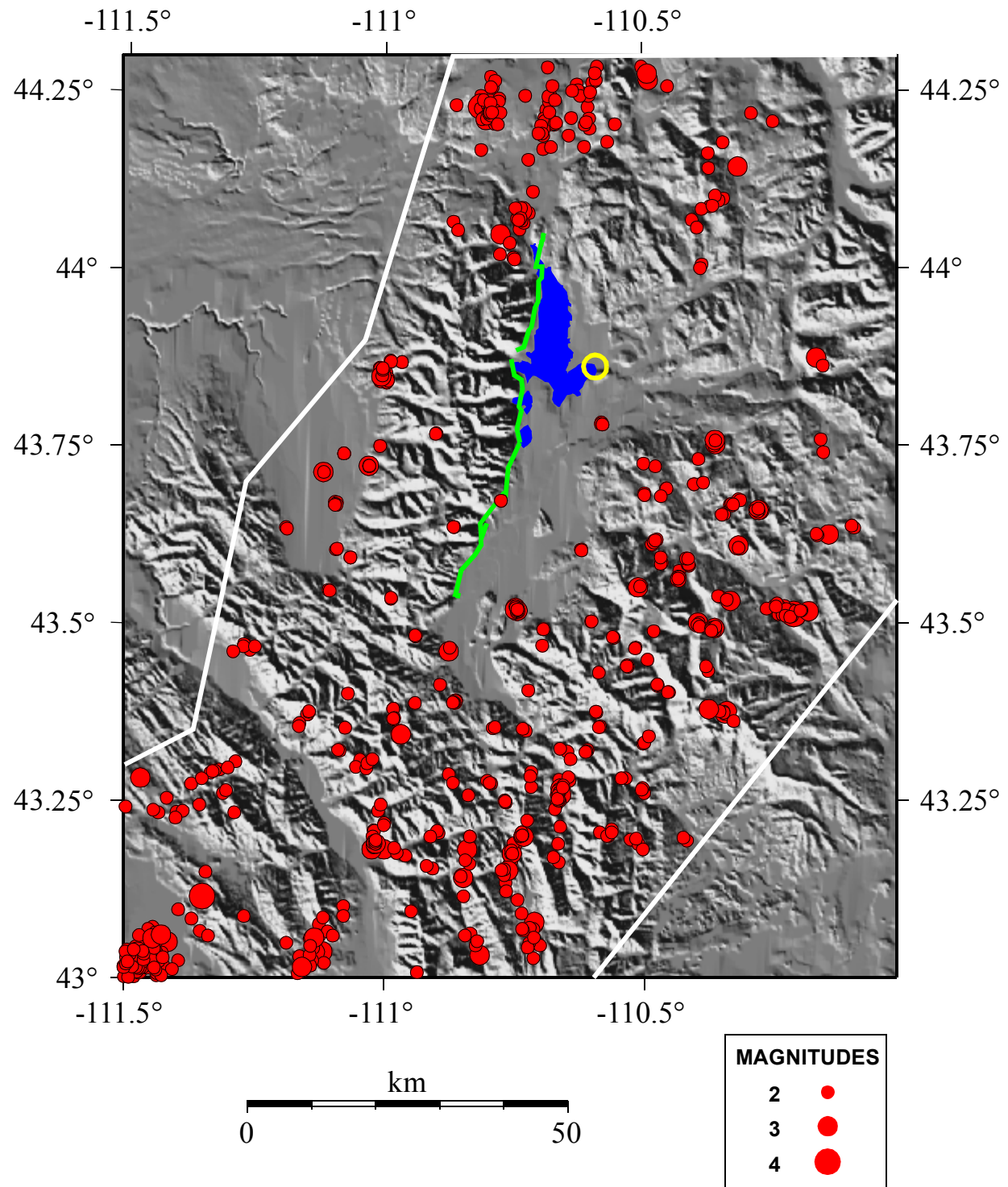


Figure 3-17: JLSN earthquakes identified as being clusters by declustering algorithm. See Figure 3-14 for plot details.

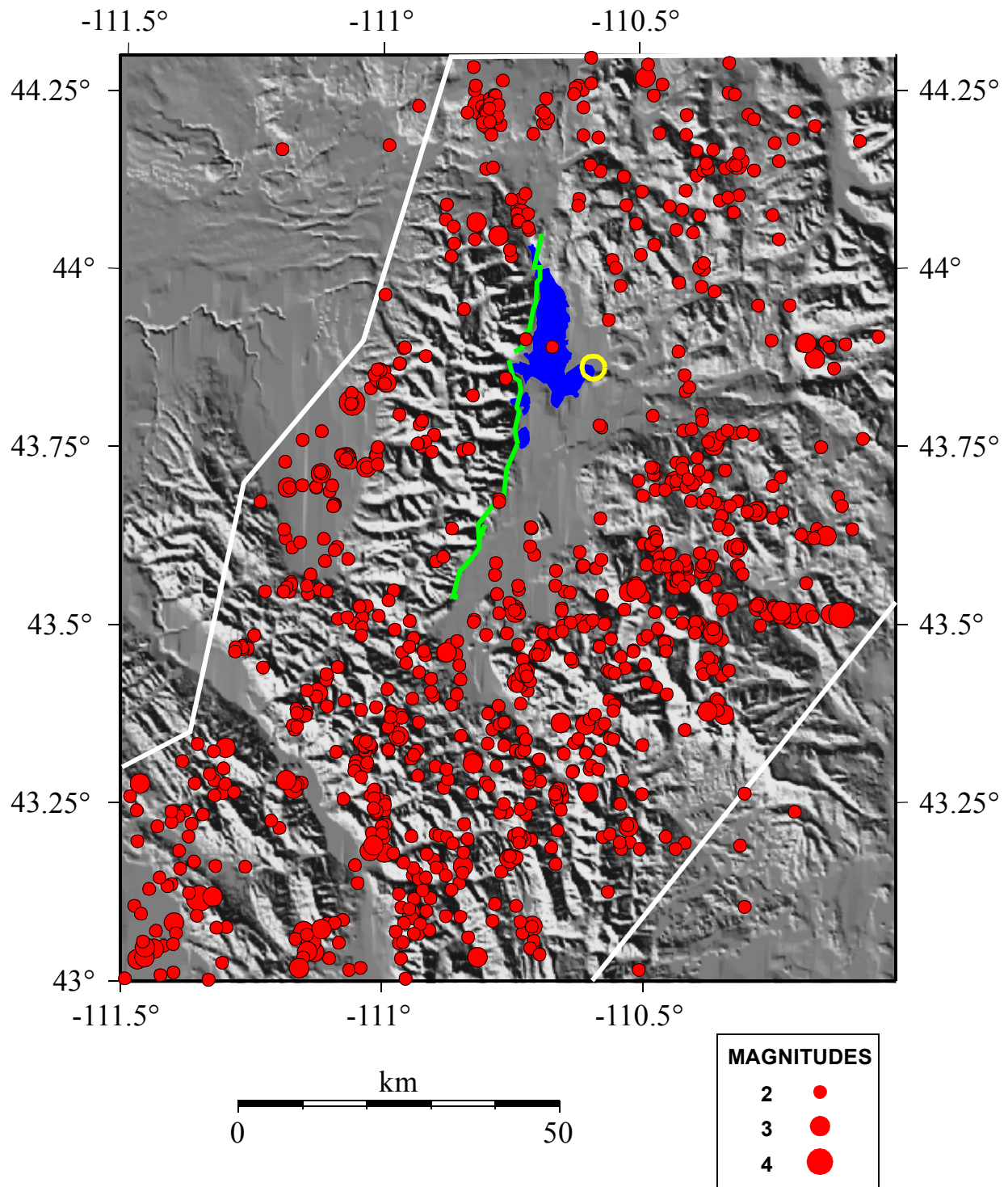


Figure 3-18: JLSN earthquakes identified as independent events by declustering algorithm. See Figure 3-14 for plot details.



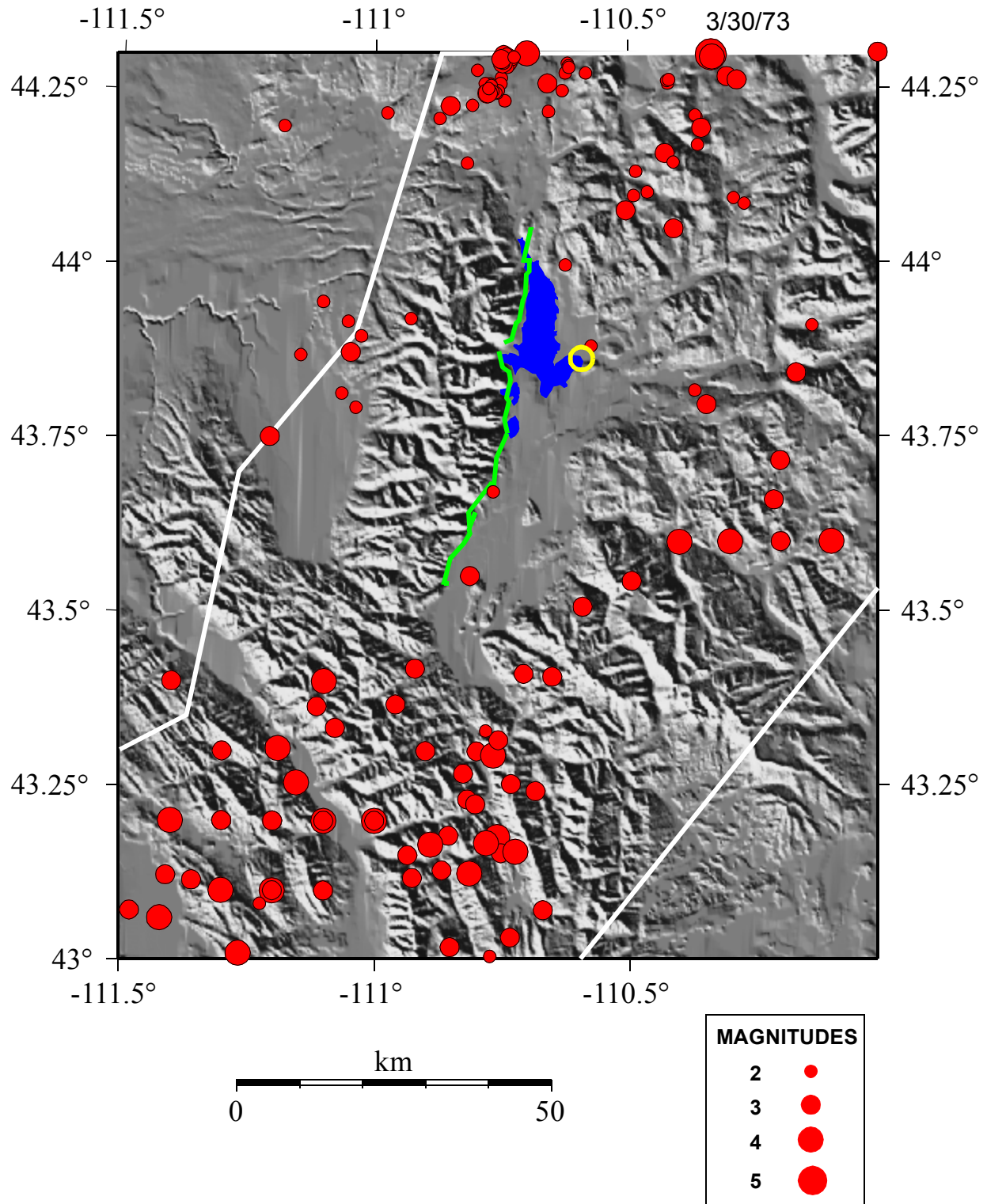


Figure 3-19: 1963 - June 1986 epicenters, from NCDEC. See Figure 3-14 for plot details.

km, in contrast to the 10 km assumed for the JLSN catalog. Of the 25 events of magnitude 4 or greater, 5 clusters and 18 independent events were identified.

### 3.5 Recurrence Calculations

Earthquake recurrence statistics were computed from the JLSN data set (1986-2001), and the combined pre-network - JLSN data set (1963-2001) shown in Figure 3-20. The maximum likelihood method (Weichert, 1980) was used, which accounts for unequal observation periods for different magnitude ranges. Data variances were computed as outlined in Weichert (1980). Recurrence parameter and seismicity rate uncertainties and confidence bounds were calculated using the method of Bollinger et al. (1989). A spacing of 0.5 magnitude unit was used. Tables 3-4a and 3-4b give the completeness periods and event counts for each data set, for the recurrence area shown in the seismicity figures (see Figure 3-14).

Incremental and cumulative recurrence curves for each data set are shown in Figures 3-21 and 3-22. Recurrence parameters  $a$  and  $b$  in the Gutenberg-Richter relation  $\text{Log}(N) = a - b(M)$ , and their uncertainties, are listed in Tables 3-5a and 3-5b. The “ $a$ ” values have been normalized to  $\text{km}^2/\text{year}$ , based on an area of  $12,872 \text{ km}^2$ . Tables 3-6a and 3-6b give observed and computed return periods for the different magnitude intervals, along with 95% confidence bounds on the maximum likelihood rates.

### 3.6 Earthquake Recurrence Discussion

Recurrence parameters for the Jackson Lake area have been computed using two data sets: JLSN data, and a combined catalog consisting of JLSN data and earthquakes recorded prior to installation of the JLSN. Each set has its advantages: the JLSN results are from high quality data that are self-consistent in location accuracy and magnitude computation, but cover a relatively short time span. The combined catalog results offer a longer time span (38 years vs. 15 years) and include more moderate (magnitude 4 and 5) events, but magnitude determinations for pre-JLSN events were computed using at least four different magnitude formulas, are of indeterminate quality, and their compatibility with JLSN magnitude values is unknown. Further use of these relations, for example in a probabilistic ground motion analysis, should incorporate both results.

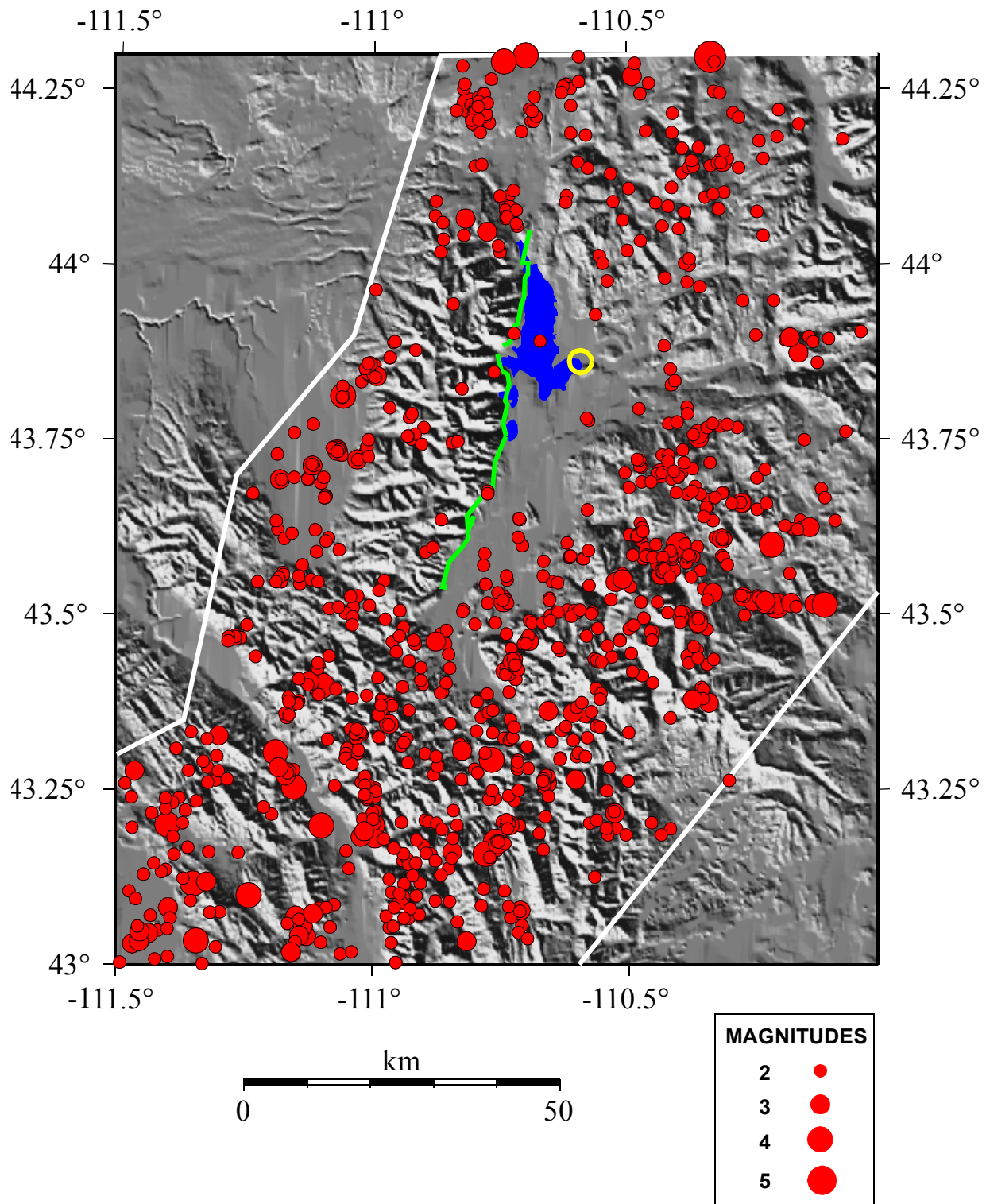


Figure 3-20: Declustered earthquakes used in recurrence calculations using the combined catalogs. See Figure 3-14 for plot details.



**Table 3-4a: Completeness Periods and Event Counts Used in Recurrence Calculations, JLSN Catalog**

Magnitude Range	Completeness Period	Number of Earthquakes
2.0 - 2.5	6/1986 - 12/2001	704
2.5 - 3.0	6/1986 - 12/2001	196
3.0 - 3.5	6/1986 - 12/2001	64
3.5 - 4.0	6/1986 - 12/2001	10
4.0 - 4.5	6/1986 - 12/2001	4
4.5 - 5.0	6/1986 - 12/2001	1
5.0 - 5.5	6/1986 - 12/2001	0
5.5 - 6.0	6/1986 - 12/2001	0
6.0 - 6.5	6/1986 - 12/2001	0

**Table 3-4b: Completeness Periods and Event Counts Used in Recurrence Calculations, JLSN and 1963-1986 Catalog**

Magnitude Range	Completeness Period	Number of Earthquakes
2.0 - 2.5*	6/1986 - 12/2001	704
2.5 - 3.0*	6/1986 - 12/2001	196
3.0 - 3.5*	6/1986 - 12/2001	64
3.5 - 4.0*	6/1986 - 12/2001	10
4.0 - 4.5	1/1963 - 12/2001	19
4.5 - 5.0	1/1963 - 12/2001	3
5.0 - 5.5	1/1963 - 12/2001	1
5.5 - 6.0	1/1963 - 12/2001	0
6.0 - 6.5	1/1963 - 12/2001	0

\* JLSN only

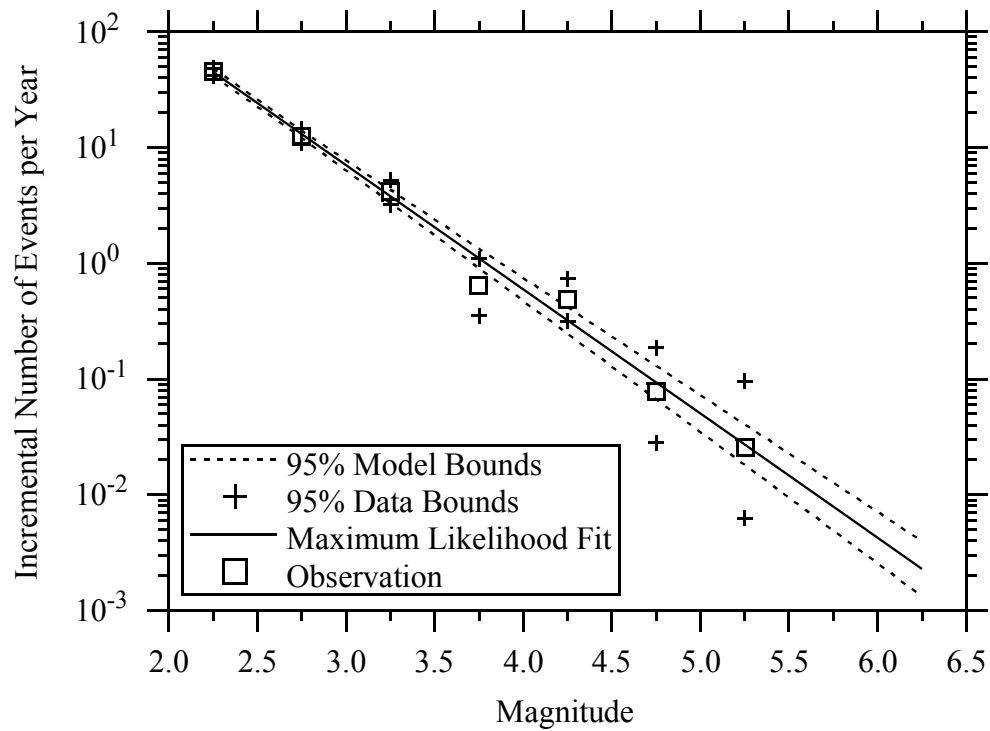


Figure 3-21a: Incremental recurrence curve for JLSN catalog.

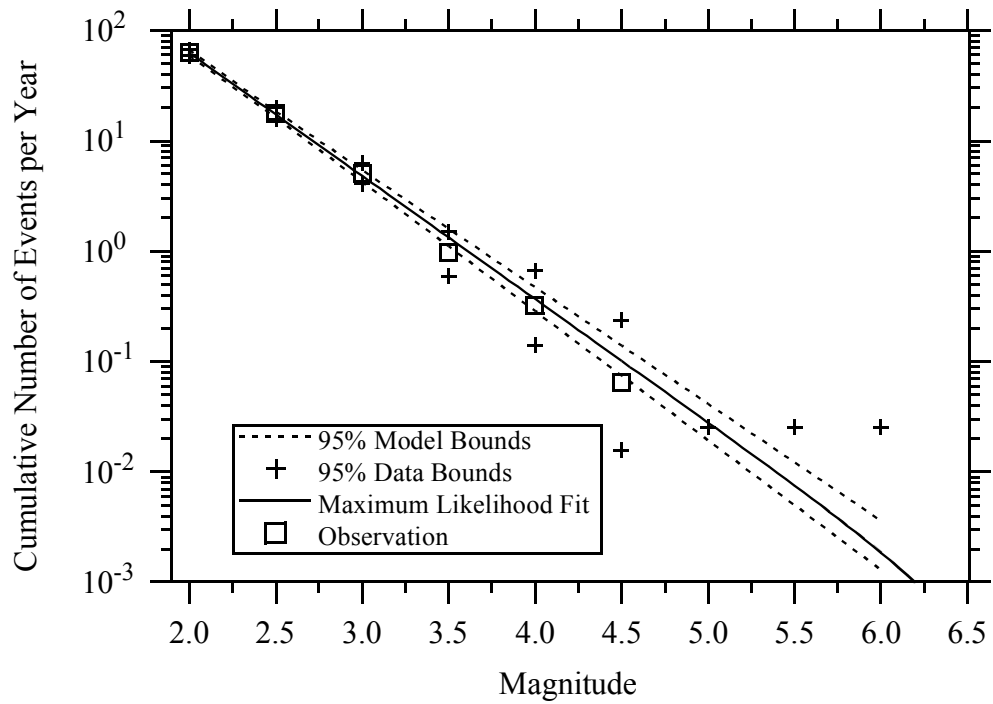


Figure 3-21b: Cumulative recurrence curve for JLSN catalog.

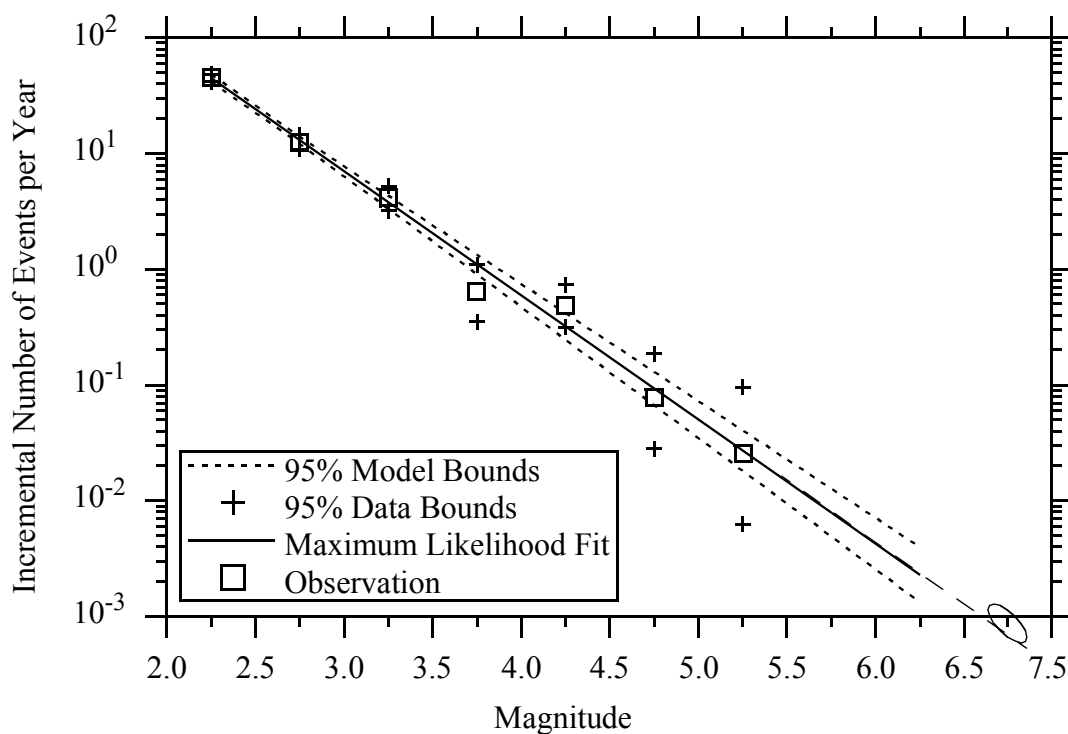


Figure 3-22a: Incremental recurrence curve for combined catalogs. The ellipse shows the approximate rate of  $M \sim 6.7-7.2$  earthquakes on the Teton fault based on Section 2.

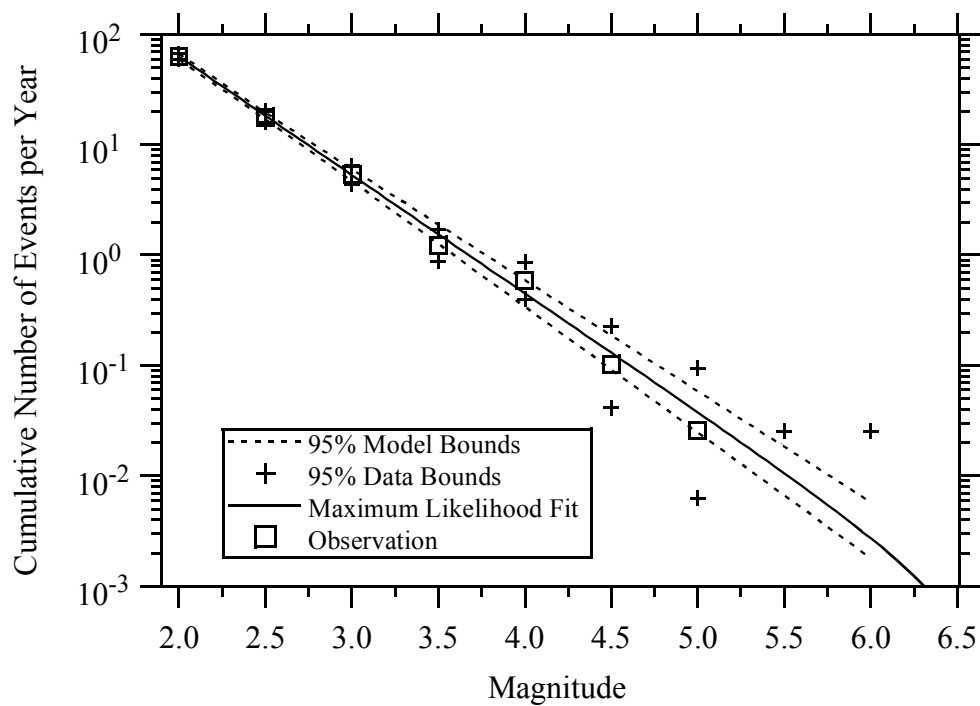


Figure 3-22b: Cumulative recurrence curve for combined catalogs.

Recurrence information from each relation, however, give a fairly consistent picture of recurrence rates of potentially hazardous randomly occurring earthquakes. The JLSN relation gives median return periods of 36 and 635 years for events greater than magnitude 5.0 and 6.0, respectively (with an upper limit of 6.5), while the combined catalog relation gives return periods of 27 and 434 years. Averaged results indicate 31 and 515 years, respectively.

Gilbert et al. (1983) obtained a recurrence relation for the Jackson Lake area which gave an (cumulative)  $a$  value of 0.86, and a  $b$  value of 1.31. This gives return periods of 38 years for magnitude  $\geq 5.0$  and 776 years for magnitude  $\geq 6.0$ ; similar to the results presented here. Wong et al. (2000) computed recurrence for a larger area of the ISB that extends from the southern Yellowstone area south to the Utah border. They obtained a cumulative  $a$  value of -1.6 (scaled to  $\text{km}^2/\text{yr}$ ) and a  $b$  value of 0.79. When scaled to our study area, this results in 27 years for magnitude  $\geq 5.0$  and 170 years for magnitude  $\geq 6.0$ . The higher activity rate for magnitude 6 events results from the inclusion of a more active section of the ISB to the south of the Jackson Lake area, and the lower  $b$  value. Piety et al. (1986) computed earthquake recurrence for the ISB from  $41^\circ\text{N}$  to  $44^\circ\text{N}$ , using a method similar to that used in this report. The results were very close to those obtained by Wong et al. (2000). Arabasz et al. (1980) computed recurrence for the ISB in Utah, based on the historic record through 1978. Their results indicated 30 years for magnitude  $\geq 5.0$  and 158 years for magnitude  $\geq 6.0$ , similar to the Wong et al. (2000) recurrence values.

**Table 3-5a: Recurrence Parameters, JLSN Catalog**

Parameter (std. dev.)	Incremental	Cumulative
$a$ ( $\sigma$ )	0.057 (.094)	-0.081 (.066)
$b$ ( $\sigma$ )	1.115 (.038)	1.115 (.030)

**Table 3-5b: Recurrence Parameters, Combined Catalogs**

Parameter (std. dev.)	Incremental	Cumulative
$a$ ( $\sigma$ )	-0.045 (.080)	-0.164 (.078)
$b$ ( $\sigma$ )	1.072 (.032)	1.0722 (.032)

**Table 3-6a: JLSN Catalog: Return Periods, Observed and Maximum Likelihood, with Upper and Lower Bounds at 95% Confidence**

Magnitude Range	Return Period (yrs) (observed)	Return Period (yrs) (maximum likelihood)	Lower Bound	Upper Bound
2.0 - 2.5	0.02	0.02	0.02	0.02
2.5 - 3.0	0.08	0.08	0.07	0.09
3.0 - 3.5	0.24	0.29	0.25	0.33
3.5 - 4.0	1.56	1.04	0.82	1.31
4.0 - 4.5	3.90	3.74	2.72	5.14
4.5 - 5.0	15.6	13.5	9.03	20.2
5.0 - 5.5	not observed	48.7	29.9	79.4
5.5 - 6.0	not observed	176	99.2	312
6.0 - 6.5	not observed	635	329	1228

**Table 3-6b: Combined Catalogs: Return Periods, Observed and Maximum Likelihood, with Upper and Lower Bounds at 95% Confidence**

Magnitude Range	Return Period (yrs) (observed)	Return Period (yrs) (maximum likelihood)	Lower Bound	Upper Bound
2.0 - 2.5	0.02	0.02	0.02	0.02
2.5 - 3.0	0.08	0.08	0.07	0.08
3.0 - 3.5	0.24	0.26	0.23	0.30
3.5 - 4.0	1.56	0.90	0.75	1.10
4.0 - 4.5	2.04	3.11	2.39	4.04
4.5 - 5.0	13.0	10.7	7.66	14.9
5.0 - 5.5	38.8	36.7	24.5	55.0
5.5 - 6.0	not observed	126	78.5	203
6.0 - 6.5	not observed	434	251	749

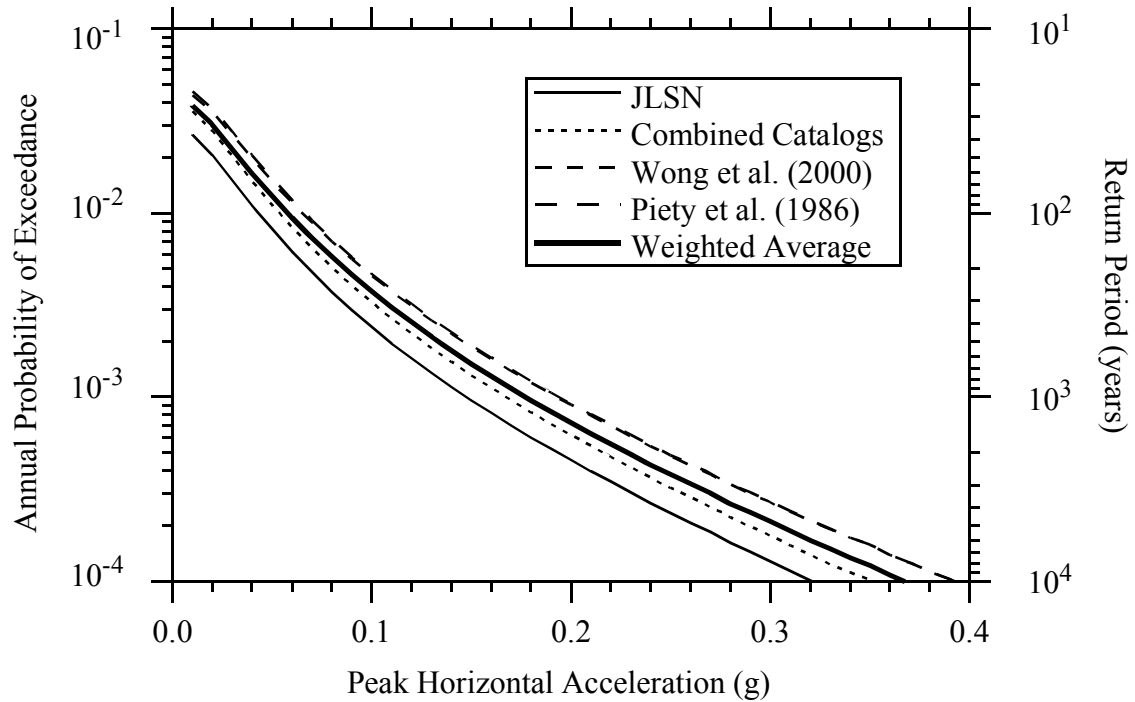


Figure 3-23a: Example soil-site hazard curves for random seismicity at Jackson Lake Dam. The three curves show differences due to different recurrence relations.

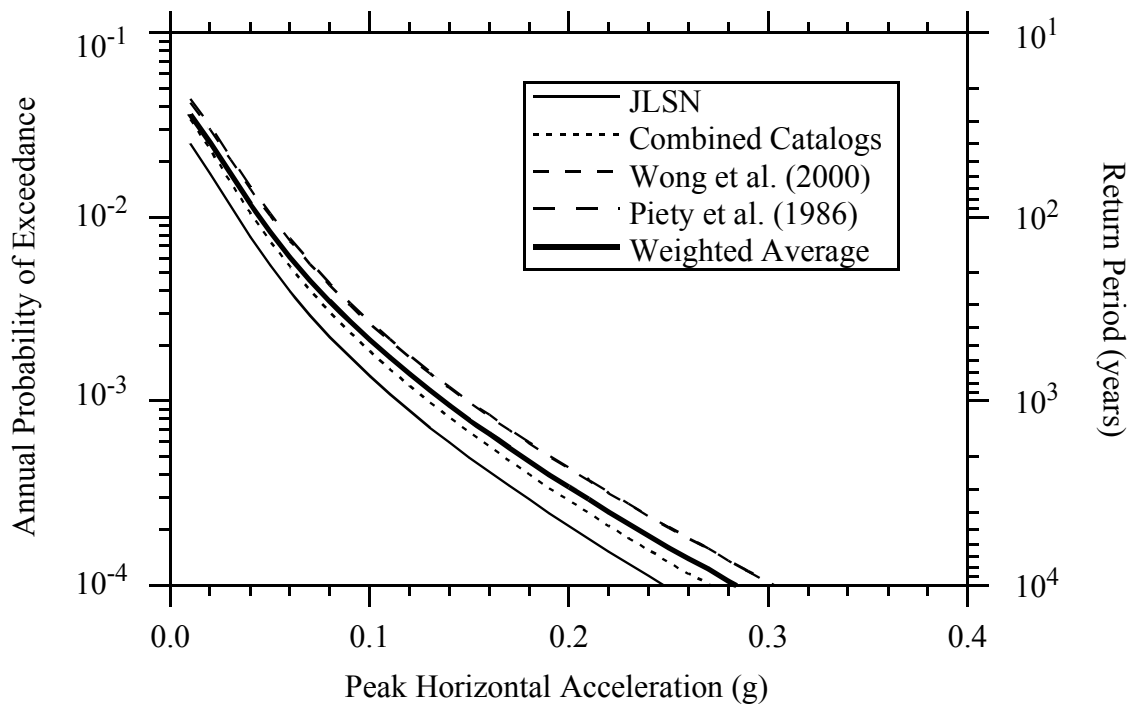


Figure 3-23b: Example rock-site hazard curves for random seismicity at Jackson Lake Dam. The three curves show differences due to different recurrence relations.

These comparisons show that for magnitude  $\geq 5.0$  events rates in the Jackson Lake area are about the same as in the ISB to the south, but for magnitude  $\geq 6.0$  events they are about 30% of the other ISB value. To show how this impacts probabilistic ground motion hazard results, Figures 3-23a and 3-23b shows example hazard curve for peak horizontal acceleration at Jackson Lake Dam for soil (Figure 3-23a) and rock (Figure 3-23b) site conditions. The four hazard curves were produced using the two recurrence curves developed in this report, the recurrence relation of Wong et al. (2000), and that of Piety et al. (1986). The soil and rock attenuation functions used are from Spudich et al. (1999). (These examples are for purposes of comparison only, and should not be used for engineering applications). Figures 3-23a and 3-23b show that the other two recurrence results gives larger ground motions; at a return period of 10,000 years in Figure 3-23a, the Wong et al. (2000) recurrence produces about 17% higher soil and rock ground motions than given by the average of the two relations developed in this report.

It is doubtful if sound physical arguments could be made as to why seismic activity is lower between 43N and 43.5N than in other parts of ISB. When observed as a whole, the ISB does form a recognizable band of seismicity, but within that band the distribution of seismicity is quite heterogeneous (e.g., Arabasz and Smith, 1980). The lower rate for  $M \geq 6$  events is in part due to the higher b-value computed here, compared to the other ISB recurrence calculations. This value appears to be real, and not the result of incomplete reporting of the smaller magnitudes (Figure 22a,b). On the other hand, there are uncertainties associated with the recurrence figures presented in this report. For example, the coda magnitude has not been calibrated to a "true" local or moment magnitude scale, and the pre-network catalog contains significant errors in earthquake locations, and several different magnitude scales. For the hazard curves shown in Figures 23a and b, we therefore weight the Wong et al. (2000) and Piety et al. (1986) relations equally with those computed for this report. The weighted hazard curves are shown in these figures. At a return period of 10,000 years, this results in 8% higher ground motions for the rock relations, and 10% higher for the soil relations, over the averaged recurrence relations for the JLSN area presented in this report.

### 3.7 Summary and Conclusions

The Jackson Lake Seismographic Network recorded 1150 well-located earthquakes between August, 1986, and May, 2002, that provided the basis for inverting for 3D P-wave crustal velocity structure near Jackson Lake Dam. The 3D P-wave velocity-hypocenter-station-correction inversion provided information necessary to locate earthquake for earthquake recurrence investigations, to constrain focal mechanisms for seismotectonic investigations, and to determine the large-scale 3D crustal P-wave velocity structure required to estimate seismic loads at Jackson Lake Dam. The 3D P-wave velocity model and corresponding station corrections obtained from the hypocenter-velocity-station correction inversion provide a much better fit to the data than that obtained with the 1D original velocity model. For all relocated events, the mean absolute P-wave arrival time residual decreased by 32%. The 3D velocity inversion revealed a low-velocity region east of the Teton fault that includes Jackson Lake Dam. The low-velocity region extends to depths of ~4 km below the dam, has the lowest velocities in the 3D P-wave velocity model (3.4 km/s), and has the largest spatial extent of any of the low-velocity regions in the 3D velocity model (Figure 3-4). While the shallowest velocities may be vertically smeared due to insufficient ray coverage, the lower boundaries of the velocity anomalies are fairly well-constrained by the data. For the Jackson Lake Dam site-response stations JLD2 to JLD7, which are located on soil sites within the 3D velocity grid, the positive station corrections indicate that the shallow local velocities are lower than those given by the 3D velocity model. The velocities in the 3D model decrease from station JLD2 on the south to station JLD7 near the northern end of Jackson Lake Dam. These results are consistent with geophysical measurements discussed in Section 5, that show extremely low-velocity materials beneath the dam that increase in thickness toward the north.

Relatively few earthquakes are located near the possible downdip projections of the Teton fault; many more earthquakes are located in the footwall side of the Teton fault. The same seismicity behavior is associated with other normal faults in the ISB, particularly the Wasatch fault system in Utah (Smith and Arabasz, 1991), the only other predominantly normal-faulting region in the ISB with sufficient seismographic station coverage to locate earthquakes with uncertainties < 5 km. Most earthquakes are < 14 km deep, but seismicity does extend to a maximum depth of ~17 km, providing a basis to assign maximum faulting depths for ground motion modeling in Section 6.



Reasonably well-constrained focal mechanisms were obtained for 773 earthquakes located by the JLSN using P-wave first motions and SV/P amplitude ratios from vertical component seismograms. The strike-slip, normal-slip, and oblique normal-slip focal mechanisms represent > 92% of the focal mechanisms and occur throughout the study area (Figures 3-10 to 3-13). *T*-axes are nearly uniformly orientated almost east-west from north grid coordinate -35 km to 40 km. Both the northeast deflection of the *T*-axes at the northern limits of the grid and the southeast deflection of the *T*-axes at the southern limits of the grid, roughly maintain the *T*-axes normal to the overall parabolic distribution of seismicity east of the Snake River Plain described in Anders et al. (1989). The reverse and oblique reverse solutions are mostly confined to the region south of 15 km north grid coordinates, and may reflect stress heterogeneity in the stepover region between the Teton fault and normal faults south of the Teton fault (e.g., Grand Valley fault and Star Valley fault). Consistent with field observations discussed in Section 2, the *T*-axes and nodal planes indicate primarily normal-slip on the central and northern sections of the Teton fault, and oblique left-lateral normal slip on the southern section of the Teton fault. The focal mechanism data, particularly the *T*-axes orientations support using a dominantly normal-slip rake to simulate ground motions associated with rupture of the central and northern segments of the Teton fault.

The relative paucity of earthquakes that could be associated with the Teton fault at depth do not provide strong constraints on fault dip. Focal mechanism solutions of earthquakes located east of the surface trace of the Teton fault dips have east-dipping nodal planes that dip from 25° to 60°. There are too few earthquakes located east of the Teton fault, with far too limited spatial coverage to provide a strong constraint on fault dip, although the spatial distribution of earthquakes is generally consistent with dips of < 50°. Waveform modeling of more of the earthquakes located east of the Teton fault may provide better constraints on Teton fault dip at depth than are currently available.

Earthquake recurrence parameters were developed for the Jackson Lake region. Two data sets were used; the Jackson Lake Seismic Network (JLSN) catalog (June, 1986 - December, 2001) with a lower magnitude cutoff of 2.0 to ensure catalog completeness, and the historic record for this region prior to the network's installation in 1986 (1963 - May, 1986). Two sets of recurrence parameters were developed, one with just the JLSN data and one with the combined JLSN -

pre-1986 information. Because no earthquakes in either catalog have been positively associated with a known fault, this seismicity represents “random” or “background” earthquakes, and any further analysis using the earthquake recurrence parameters developed here pertain only to such seismic activity. The earthquake catalogs were declustered to produce a total of 984 independent events in the JLSN catalog and 18 independent events in the pre-JLSN catalog.

Each earthquake dataset has its advantages: the JLSN results are from high quality data that are self-consistent in location accuracy and magnitude computation, but cover a relatively short time span. The combined catalog results offer a longer time span (38 years vs. 15 years) and include more moderate (magnitude 4 and 5) events, but magnitude determinations for pre-JLSN events were computed using at least four different magnitude formulas, are of indeterminate quality, and their compatibility with JLSN magnitude values is unknown. Further use of these relations, for example in a probabilistic ground motion analysis, should incorporate both results. Recurrence information from each relation, however, give a fairly consistent picture of recurrence rates of potentially hazardous randomly occurring earthquakes. The JLSN relation gives median return periods of 36 and 635 years for events greater than magnitude 5.0 and 6.0, respectively (with an upper limit of 6.5), while the combined catalog relation gives return periods of 27 and 434 years. Averaged results indicate 31 and 515 years, respectively.

Gilbert et al. (1983) obtained a recurrence relation for the Jackson Lake area which gives return periods of 38 years for magnitude  $\geq 5.0$  and 776 years for magnitude  $\geq 6.0$ ; similar to the results presented here. Wong et al. (2000) computed recurrence for a larger area of the ISB that extends from the southern Yellowstone area south to the Utah border. When scaled to our study area, this results in 27 years for magnitude  $\geq 5.0$  and 170 years for magnitude  $\geq 6.0$ . The higher activity rate for magnitude 6 events in Wong et al. (2000) results from the inclusion of a more active section of the ISB to the south of the Jackson Lake area, and their lower  $b$  value. Piety et al. (1986) computed earthquake recurrence for the ISB from  $41^{\circ}\text{N}$  to  $44^{\circ}\text{N}$ , using a method similar to that used in this report. The results were very close to those obtained by Wong et al. (2000). Arabasz et al. (1980) computed recurrence for the ISB in Utah, based on the historic record through 1978. Their results indicated 30 years for magnitude  $\geq 5.0$  and 158 years for magnitude  $\geq 6.0$ , similar to the Wong et al. (2000) recurrence values.

Hazard curves for peak horizontal acceleration were computed, using a single attenuation function and the recurrence relations developed in this report, and those of Wong et al. (2000) and Piety et al. (1986). A weighted curve was calculated, with the results of the two recurrence relations developed here and those of the other ISB relations weighted equally. The computed ground motions of the averaged relations, at a 10,000 year return period, are 10% or less higher than those computed from the relations developed in this report.

This section has focused on analyses related to seismicity. The 3D P-wave velocity model developed in this section serves as the basis for the more detailed crustal velocity structure modeling necessary to estimate ground motions at Jackson Lake Dam, as presented in the next section.

